Chapter 8
Cavity-Enhanced Direct Frequency Comb Spectroscopy

P. Masłowski, K.C. Cossel, A. Foltynowicz, and J. Ye

Abstract In less than fifteen years since the development of the first optical frequency comb (OFC), the device has revolutionized numerous research fields. In spectroscopy, the unique properties of the OFC spectrum enable simultaneous acquisition of broadband spectra while also providing high spectral resolution. Due to the regular structure of its spectrum, an OFC can be efficiently coupled to an optical enhancement cavity, resulting in vastly increased effective interaction length with the sample and absorption sensitivities as low as 1.3×10^{-11} $\mathrm{cm}^{-1}\,\mathrm{Hz}^{-1/2}$ per spectral element. This technique, called cavity-enhanced direct frequency comb spectroscopy (CE-DFCS), provides ultra-sensitive absorption measurements simultaneously over a wide spectral range and with acquisition times shorter than a second.

This chapter introduces the main ideas behind CE-DFCS including properties of various comb sources, methods of coupling and locking the OFC to the enhancement cavity, and schemes for broadband, simultaneous detection. Examples of experimental implementations are given, and a survey of applications taking advantage of the rapid, massively parallel acquisition is presented.

8.1 Introduction

An optical frequency comb (OFC) [1–8] can be defined in the frequency domain as a series of narrow, equally spaced lines with a known, and controllable, optical frequency and a well-defined phase relationship between them. A frequency comb

P. Masłowski (✉)
Institute of Physics, Faculty of Physics, Astronomy and Informatics, Nicolaus Copernicus University, Grudziadzka 5, 87-100 Torun, Poland
e-mail: pima@fizyka.umk.pl

K.C. Cossel · J. Ye
JILA, National Institute of Standards and Technology and University of Colorado, Department of Physics, University of Colorado, Boulder, CO 80309-0440, USA

A. Foltynowicz
Department of Physics, Umeå University, 901 87 Umeå, Sweden

G. Gagliardi, H.-P. Loock (eds.), *Cavity-Enhanced Spectroscopy and Sensing*,
Springer Series in Optical Sciences 179, DOI 10.1007/978-3-642-40003-2_8,

in the spectral domain originates from an interference of a train of equally spaced pulses in the time domain. The frequency spacing between adjacent lines—called comb modes—in the frequency domain is given by the inverse of the time between two consecutive pulses. This frequency is called the repetition rate (f_{rep}) and is determined by the optical path-length inside the laser resonator. The inverse of the duration of each pulse sets the frequency domain spectral bandwidth. There exists one additional degree of freedom, which is the pulse-to-pulse phase shift of the electric-field carrier wave relative to the pulse envelope (the carrier-envelope phase shift, $\Delta\varphi_{\mathrm{CE}}$). This shifts the comb modes in the frequency domain such that the frequency of the mth mode is given by $\nu_m = mf_{\mathrm{rep}} + f_0$. Here m is an integer mode number, and f_0 is the offset frequency (also called the carrier-envelope offset frequency) due to the carrier-envelope phase shift, given by $f_0 = f_{\mathrm{rep}}\Delta\varphi_{\mathrm{CE}}/(2\pi)$.

Optical frequency combs were initially developed for frequency and time metrology [6, 7]. Due to both the uniformity of the frequency comb mode spacing at the 10^{-19} level [9] and the possibility to stabilize individual modes to below 10^{-15} fractional frequency stability [4, 10–12], they have indeed revolutionized the field. Today, OFCs allow precise and yet relatively easy metrology of optical frequencies without the need for complicated frequency chains [3, 4] and enable the transfer of frequency stability and phase coherence over long distances [13–17] or to different spectral regions [11, 18]. In a relatively short period of time, frequency combs have found numerous applications in a variety of scientific fields [8, 19] such as astronomy [20–24], bioengineering [25, 26], and microwave generation for communication systems, deep space navigation and novel imaging [27, 28]. They have helped discover properties of physical objects ranging in size from atoms [29–31] to planets and planetary systems [23].

With the capability for precise measurement of the optical frequencies provided by the OFCs, it was natural to consider their application to laser spectroscopy [29]. Continuous wave (cw-) laser spectroscopy referenced to a frequency comb provides significantly increased frequency precision and accuracy [1, 32–37], promising exciting improvements in the determination of fundamental constants [29, 33, 38–41]. However, to fully exploit the unique properties of the comb spectrum, an OFC can be used directly as the light source for spectroscopy, in an approach called direct frequency comb spectroscopy (DFCS), first introduced in Ref. [30]. In this technique, precise control of the frequency comb structure is used to simultaneously interrogate a multitude of atomic or molecular levels or to study time-dependent quantum coherence [30, 31, 42]. The frequency comb spectrum provides several benefits for spectroscopic applications when compared to more commonly used sources such as incoherent (thermal or LED) light or cw lasers [43–45]. The broad emission spectrum (broader than emission spectra of some incoherent sources) allows simultaneous acquisition over thousands of channels, facilitating the measurement of different spectroscopic features at the same time. The main advantage lies in the fact that this broadband operation is combined with high spectral resolution, fundamentally limited only by the linewidth of a single comb tooth, which can be as narrow as below 1 Hz [10, 11]. Comb spectroscopy thus maintains the high resolution of cw-laser-based spectroscopy, while removing the need for time-consuming, and often troublesome, frequency scanning.

Due to the spatial coherence of the frequency comb sources, the detection sensitivity for DFCS can be significantly enhanced by extending the path length of the optical beam through the absorbing sample. Absorption cells of moderate lengths with geometrical designs providing tens to hundreds of passes are widely used in cw-laser spectroscopy [46, 47] and can be used with DFCS as well [48, 49], enabling broadband, parallel signal acquisition with moderate sensitivity. One advantage is that the metallic mirror coatings allow the entire OFC spectrum to be used for spectroscopic interrogation [48]. In addition, since no resonance condition exists, these systems allow straightforward optical coupling of the comb spectrum. These features make multipass cells suitable for future commercial spectrometers with intermediate sensitivities based on broadband femtosecond laser sources.

For more demanding applications such as breath analysis, atmospheric research, or detection of hazardous substances, the required concentration detection limits are often lower than those obtainable with multipass cells. A further increase of the interaction length between the laser beam and a gaseous sample can be obtained with a high-finesse optical enhancement cavity. The interaction length inside the cavity can be increased by a factor of tens-of-thousands, providing superb absorption sensitivity. In the 1990's researchers working on cavity ring down spectroscopy started to experiment with coupling of picosecond lasers into passive optical cavities [50]. The very limited spectral coverage of a picosecond laser made it unnecessary to consider the carrier-envelope offset frequency of a comb (a concept that was matured only after the invention of optical frequency combs at the turn of the century), and hence only the matching between the repetition frequency and the cavity free spectral range (*FSR*) was considered. When this approach was naturally extended to femtosecond mode-locked lasers, termed mode-locked laser cavity-enhanced absorption spectroscopy (ML-CEAS) [51], the authors operationally found a "magic point"—the cavity length for which the coupling was most efficient (i.e. where f_{rep} and the FSR were matched). Rigorous analysis of comb-cavity coupling, which included the concept of the adjustment of the carrier-envelope offset frequency, was first provided in Ref. [52]. This knowledge led to the demonstration in 2006 of cavity-enhanced direct frequency comb spectroscopy (CE-DFCS) [53], which delivers sensitivities beyond the capabilities of traditional Fourier-transform spectroscopy (FTS)—the workhorse of broadband molecular spectroscopy. The potential of CE-DFCS has already been demonstrated for detection of molecular species important for environmental research [48, 53–55], monitoring of production processes [56], and human breath analysis [57], as well as for analysis of the energy level structure of exotic molecules [58, 59], and tomography of supersonic jet expansion [60]. The number of applications is constantly growing, triggered by the continuing development of frequency comb sources covering new spectral domains ranging from the extreme ultraviolet (EUV) [61–64], through the UV, visible, and extending to the mid-infrared (mid-IR) [65–70].

The aim of this chapter is to introduce the reader to the rapidly evolving technique of CE-DFCS and to review the existing approaches and experimental setups. Various OFC sources are presented, including the most common Ti:sapphire and fiber-based lasers, as well as those based on nonlinear frequency conversion working in

various spectral ranges. In addition, a comparison of laser sources used for spectroscopic applications is given. Next, schemes for coupling and locking an OFC to an enhancement cavity are discussed. A variety of broadband detection approaches are introduced along with examples of the existing experimental configurations. Finally, a few CE-DFCS applications are presented to demonstrate the unique capabilities of this broadband spectroscopic technique.

8.2 Frequency Comb Sources

Frequency combs can be generated by a variety of laser sources, which can be divided into three general categories: mode-locked lasers, indirect sources, and cw-laser based sources. Mode-locked lasers, which emit trains of ultrashort pulses, can produce frequency combs directly at the output of the laser when their frequency domain structure is controlled and stabilized [1–3, 71, 72]. Such precise control has only been reliably accomplished in a small subset of all mode-locked lasers, and we focus our attention on the most common of those gain media, namely: Ti^{3+}:sapphire, Yb^{3+}:fiber, Er^{3+}:fiber, Tm^{3+}:fiber, and Cr^{2+}:ZnSe. Indirect sources use nonlinear optical effects to modify or shift the spectrum of a mode-locked laser. Cw-laser based sources use nonlinear or electro-optical materials to generate multiple sidebands from a cw laser. Below we provide an overview of how each of these types of sources work and briefly discuss some common features and their relative advantages and disadvantages.

The first consideration when choosing a comb source suitable for a particular application is usually its spectral coverage. For molecular spectroscopy, the strongest transitions, and thus the highest detection sensitivity, exist in the visible to ultraviolet (electronic transitions) and in the mid-infrared (fundamental vibrational modes) wavelength ranges. Many interesting atomic transitions, such as the 1S–2S transition in He or He-like ions or nuclear transitions in Th or U, occur below 200 nm. This has pushed the development of comb sources towards all of these spectral regions. Other important factors to consider when choosing a comb source are the available bandwidth, output power, and repetition rate. A broad spectral bandwidth is desired for multi-species detection; however, for a given laser power and repetition rate, a broader bandwidth results in a lower power per comb line, potentially decreasing the detection sensitivity, depending on the efficiency of the read-out method. Higher repetition rate provides higher power per comb line, but if the spacing of the comb lines is larger than the width of individual spectral features, the comb lines must be scanned to cover the full spectrum. Finally, for applications outside of spectroscopy labs, the robustness and portability of the system also need to be considered. These trade-offs have led to the development of a wide range of comb sources as illustrated in Fig. 8.1. This figure shows that it is now possible to find a comb source at any wavelength between the deep-UV and the mid-IR.

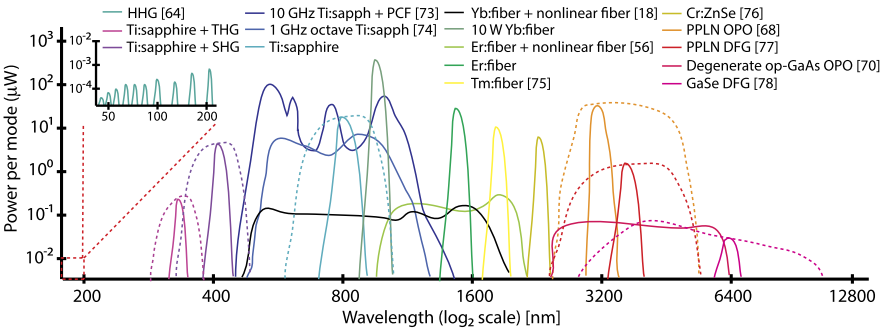

Fig. 8.1 Comparison of the operating spectral range and the output power of different comb sources. *Dashed curves* indicate the tuning range for tunable sources. Descriptions of the systems can be found in the text. HHG—high harmonic generation; THG—third harmonic generation; SHG—second-harmonic generation; PCF—photonic crystal fiber; PPLN—periodically-poled lithium niobate; OPO—optical parametric oscillator; DFG—difference frequency generation; op-GaAs—orientation-patterned gallium arsenide; GaSe—gallium selenide

8.2.1 Mode-Locked Lasers

Over the past few decades mode-locked operation has been achieved in many different gain media, including solid-state lasers, dye lasers, fiber lasers, and diode lasers. Several mechanisms exist for mode-locking these lasers [79–81], and they can be broadly divided into active or passive methods.

Active Mode-Locking Active mode-locking is obtained by forcing multiple modes of a laser resonator to lase with a well-defined phase relation between them [81]. This can be accomplished with an intra-cavity electro-optic or acousto-optic modulator that is driven at f_{rep} (i.e., at the desired comb mode spacing, determined by the optical path-length of the laser cavity). Thus, laser light at one mode will have sidebands located at adjacent modes. These sidebands will experience gain and will produce their own sidebands, which results in a cascaded generation of laser modes with fixed phases. While active mode-locking is very robust, it cannot produce extremely short pulses due to the limited bandwidth of active modulators. Because of this limitation, most comb sources rely on some form of passive mode-locking instead of, or in addition to, active mode-locking.

Passive Mode-Locking: Saturable Absorber Passive mode-locking is achieved by modifying the temporal response of the laser cavity to favor pulse formation over cw lasing. One way to accomplish this is to incorporate an intra-cavity absorbing medium with an absorption coefficient given by

$$\alpha = \frac{\alpha_0}{1 + \frac{I}{I_s}}, \tag{8.1}$$

where α_0 is the zero-power absorption coefficient, I is the intra-cavity intensity, and I_s is the saturation intensity. The intensity-dependent absorption has the effect

of reducing the power of the leading edge of a pulse relative to the peak of the pulse. The carrier lifetime of common saturable absorbers is in the range of picoseconds to nanoseconds, which would limit the achievable pulse duration to this time scale; however, when combined with gain saturation to reduce the gain for the trailing edge of the pulse, it is possible to generate shorter pulses.

The most common saturable absorbers are semiconductor-based quantum wells (such as GaAs or InGaAsP) grown on the surface of Bragg reflecting mirrors [82]. These are called either saturable Bragg reflectors (SBRs) or semiconductor saturable absorber mirrors (SESAMs) and are typically used as an end-mirror (at the focus of a lens) in the laser cavity. To overcome some of the limitations (such as carrier lifetime) of semiconductor-based saturable absorbers and to extend the applicability to other wavelength regions, saturable absorbers based on materials such as carbon nanotubes and graphene have been demonstrated [83–85].

Passive Mode-Locking: Kerr Effect An optical field (E) induces a polarization (P) in a material given by $P = \chi_e E$, where χ_e is the material susceptibility [86]. For strong fields, χ_e exhibits a nonlinear behavior $\chi_e \approx \chi^{(1)} + \chi^{(2)}E + \chi^{(3)}E^2 + \cdots$. For a material with inversion symmetry (and for all amorphous materials), $\chi^{(2)} = 0$. Using $I = (cn_0\varepsilon_0|E|^2)/2$ and $n^2 = 1 + \chi_e$, where c is the speed of light, n_0 is the refractive index in vacuum and ε_0 is the vacuum permittivity, the refractive index is given by $n \approx n_0 + n_2 I$ for small $\chi^{(3)}$. The nonlinear index n_2 is proportional to $\chi^{(3)}$. This (instantaneous) modification of the index of refraction as a function of intensity is known as the Kerr effect.

In solid-state lasers such as Ti:sapphire [87, 88] and Cr:ZnSe [89–91], the Kerr effect results in a nonlinear phase that varies as a function of the radial position across the beam profile [81, 92]

$$\phi_{nl}(r,t) = \left(\frac{2\pi}{\lambda}\right) n_2 d I(t) e^{-\left(\frac{2r^2}{w_o^2}\right)} \approx \left(\frac{2\pi}{\lambda}\right) n_2 d I(t) \left(1 - 2\frac{r^2}{w_o^2}\right), \tag{8.2}$$

for a thin material of thickness d and a Gaussian beam of waist w_o. This parabolic phase front results in an effective lens of focal length

$$f = \frac{w_o^2}{4 n_2 d I_0}, \tag{8.3}$$

where I_0 is the peak pulse intensity. This dynamic lens can be used as an effective saturable absorber for mode-locking (called Kerr-lens mode-locking or KLM) in several ways. First, with an addition of a geometrical aperture inside the laser cavity, the transmission through the aperture will increase with more dynamic lensing, so the net gain will be higher for shorter pulses. Even without a hard aperture, the presence of the Kerr lens modifies the cavity parameters. Thus a cavity near or beyond the stability edge for cw operation can be made more stable for pulsed operation. KLM lasers may not be self-starting, but typically a small perturbation is sufficient to initiate mode-locking. Because the Kerr effect is instantaneous, the pulse duration is only limited by intra-cavity dispersion or fundamentally by the

gain bandwidth of the crystal. In general, KLM lasers provide the shortest pulse durations achievable directly from the gain medium.

The Kerr effect also occurs in Yb- and Er-doped gain fibers where it results in a nonlinear rotation of elliptically polarized light. This polarization rotation can be used in a ring cavity with polarization selective elements to achieve mode-locking by increasing the transmission for pulsed light through an intra-cavity polarizer [93]. Polarization-rotation mode-locking can be used to create all-fiber femtosecond lasers with no free-space sections, providing reliable, self-starting mode-locked operation.

8.2.2 Indirect Sources

The ability to produce ultrashort pulses from mode-locked lasers results in high peak intensity per pulse. This enables efficient use of nonlinear effects in many optical materials to broaden or shift the spectrum of a mode-locked laser. Frequency combs can thus be generated in spectral regions that are impossible or difficult to access with cw lasers, such as the extreme ultraviolet (below 100 nm) or the mid-infrared (2–10 μm). In addition, frequency combs can simultaneously cover multiple octaves of spectral bandwidth using nonlinear optical effects, far exceeding the tuning range of any cw lasers, while still maintaining the same high-resolution capability. This flexibility makes indirect comb sources well suited for new applications in spectroscopy.

Many optical crystals do not possess inversion symmetry and they therefore exhibit $\chi^{(2)}$ nonlinearity, which can be used for second-harmonic generation (SHG), sum-frequency generation (SFG), difference-frequency generation (DFG), and parametric generation [86]. Phase matching between three optical frequencies must be satisfied in all of these processes; this can be accomplished by using different axes of a birefringent crystal and tuning the input angle and polarization relative to the crystal axes. Alternatively, a crystal can be periodically poled such that the phase walk-off is periodically corrected, thus maintaining phase matching over many wavelengths. Periodically-poled materials can have "fan-out" poling-periods that vary linearly across one dimension of the crystal so that the operating (phase-matched) wavelength can be tuned by translating the crystal. In addition, longer periodically-poled crystals can be used without severely limiting the angular acceptance range (and thus the phase-matched spectral bandwidth), resulting in higher conversion efficiencies.

Large nonlinear effects can also be obtained by tight confinement of an optical field in small-core optical fibers [94, 95] (such as photonic crystal fiber [96, 97], microstructure fiber [98, 99], and highly nonlinear fiber [100]). These fibers provide not only high peak intensities due to the small mode size but also long interaction lengths for nonlinear effects to accumulate. In addition, the dispersion profile of a fiber can be tailored by adjusting the mode size and by varying dopants, which provides more control over the existing nonlinear effects. For these reasons,

fiber-based coherent supercontinuum sources can be designed to cover over 1.5 octaves of spectral bandwidth [18] or to produce light in specific spectral regions. Currently, fibers with large nonlinearities are readily available throughout the visible and near-infrared wavelength ranges, enabling comb generation from 400 nm to 2100 nm, and have recently been demonstrated in the mid-infrared range [101–106]. The spectrum obtained from a nonlinear fiber results from a complex interplay of multiple $\chi^{(3)}$ processes including self-phase modulation, cross-phase modulation, stimulated Raman scattering, and four-wave mixing [94, 95, 107, 108]. Because of this complexity, fiber supercontinuum sources are often modeled numerically using a generalized nonlinear Schrödinger equation [94, 101].

Frequency combs operating at very short wavelengths (below 100 nm) can only be produced through the process of high-harmonic generation (HHG). With extremely high peak electric fields, like those attainable at a tight focus in an optical cavity, the perturbative expansion to the polarizability breaks down and the medium (e.g., a jet of a noble gas) is ionized. The electron is accelerated away from the atom for some period of time until the electric field reverses and accelerates the electron back toward the atom. The electron can then recombine with the atom, emitting all of the excess energy gained from the field in high-order (odd) harmonics of the original laser frequency [109–113]. The HHG process has been used to produce combs in the vacuum ultra-violet (VUV, 100 to 200 nm) and extreme ultra-violet (XUV, below 100 nm) [61, 62, 114] with over 100 μW of average power per harmonic order [115]. Very recently, high-resolution spectroscopy with an XUV comb was demonstrated, conclusively demonstrating the coherence of the HHG process [64].

8.2.3 Other Types of OFC Sources

Other types of comb sources, including these based on continuous-wave lasers, have not seen many applications in spectroscopy and are therefore only mentioned here briefly. It is possible to make a frequency comb simply by applying a strong frequency modulation to the carrier frequency, which creates sidebands at harmonics of the modulation frequency [116–119]. With very strong modulation it is possible to put optical power into high-order sidebands, resulting in a comb in the frequency domain. However, in practice, the achievable spectral bandwidth is small and thus does not provide much of an advantage over cw laser spectroscopy.

Frequency combs can also be generated by driving Raman transitions between rotational levels in molecules using two (possibly pulsed) laser frequencies. With enough Raman gain, it is possible to cascade this process and produce an octave-spanning comb [120]. These combs have only been demonstrated with large mode spacing (given by the rotational spacing of the molecules used), which potentially limits their usefulness for spectroscopy.

Recently, frequency combs based on parametric frequency conversion of cw-lasers in microresonators have been demonstrated [121–123]. When a cw laser is injected into a high-finesse microresonator, the high intra-cavity intensity results in

cascaded four-wave mixing and can generate a comb with a repetition rate set by the free spectral range of the microresonator at the pump wavelength. These sources show some interesting potential for spectroscopic applications due to their compact size and inherent simplicity; however, they are currently limited to repetition rates above 20 GHz. In addition, while mode-locking of microresonator sources has been demonstrated very recently [124, 125], the inherent noise properties of the generated comb are not yet completely understood or controllable [126, 127].

8.2.4 Typical Comb Sources

Ti:Sapphire The first realization of a fully-stabilized frequency comb was based on a mode-locked Ti:sapphire laser. These lasers, which are still widely used as comb sources, are usually Kerr-lens mode-locked. Their extremely broad gain bandwidth enables generation of ultrashort (10 fs) pulses and correspondingly large spectral bandwidth (covering about 700 nm to 1050 nm) directly from the laser. It is even possible to generate octave-spanning spectra directly from the laser with intracavity self-phase modulation [74, 128]. Meanwhile, systems offering longer pulses and thus narrower bandwidth, but widely tunable in the entire gain range, are readily available. Ti:sapphire combs can be made with repetition rates ranging from below 100 MHz up to 10 GHz [129], providing large flexibility for different applications. By the use of SHG [55] or supercontinuum fibers [96, 97] they provide high power tunable combs in the visible to UV ranges. Unfortunately, the free-space cavity of a Ti:Sapphire laser limits the robustness of this type of comb. In addition, the pump laser is still expensive and relatively bulky, further limiting the field applicability of the system.

Yb:Fiber Yb:fiber lasers [79] produce combs directly in the 1000 to 1100 nm spectral region. These lasers are typically mode-locked using a saturable absorber and are limited in spectral bandwidth (and thus in pulse duration, which is limited to about 80 fs) by the gain bandwidth of the fiber. A common configuration, illustrated in Fig. 8.2(a), consists of a linear cavity with a pump diode coupled to the gain fiber via a wavelength-division multiplexer (WDM), a fiber Bragg grating (FBG) acting as one cavity mirror (the output coupler), and a short free-space section containing a waveplate, focusing lens and saturable Bragg reflector. This design is very robust since the pump is entirely fiber-coupled and the cavity consists mostly of fiber. Additionally, the pump diodes are compact and fairly inexpensive. It is also possible to use only polarization rotation mode-locking; however, in this case free-space intracavity gratings are required for dispersion compensation. Yb:fiber combs have been built with repetition rates up to 1 GHz [131]. Yb:fiber based amplifiers are excellent for power scaling due to the high doping possible in large mode area fibers. In fact, chirped-pulse amplifiers have been used to produce a comb with 80 W average power at f_{rep} equal to 150 MHz [130]. One drawback of Yb:fiber lasers is that, due to the narrow gain bandwidth, they are not very tunable without external spectral broadening; however, the high power enables efficient nonlinear optics.

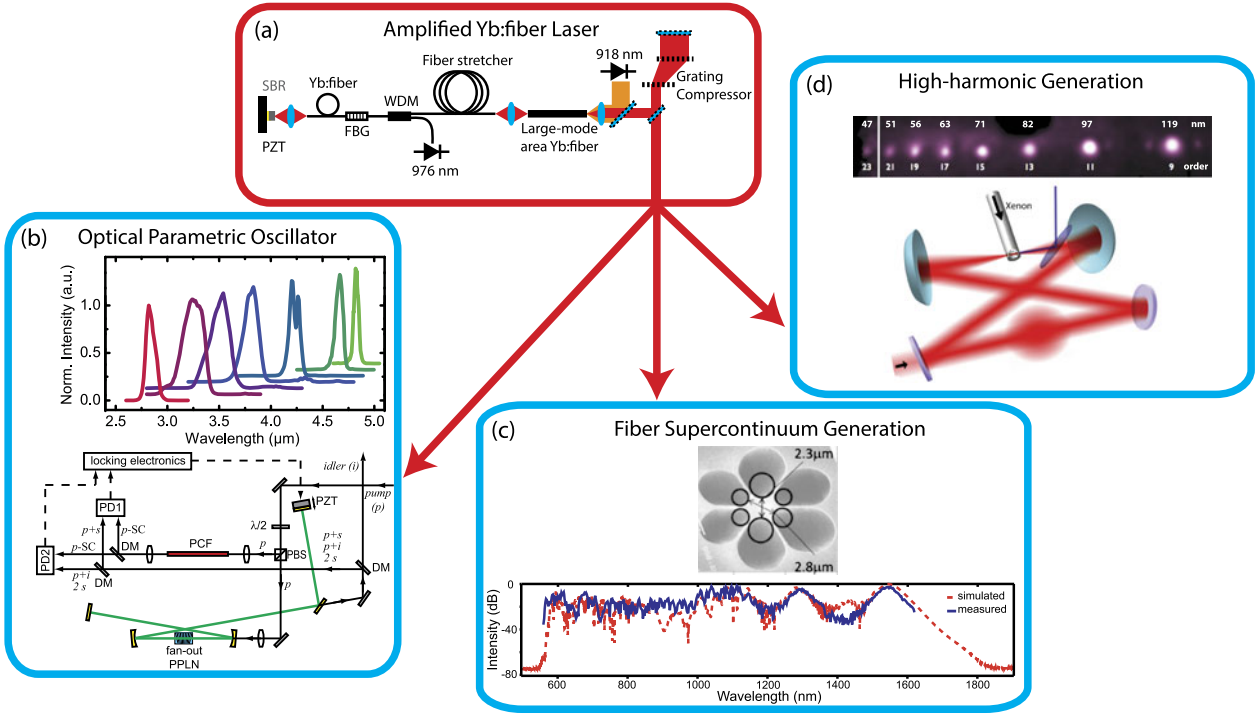

Fig. 8.2 Frequency comb sources at different spectral regions based on a Yb:fiber laser at 1.06 μm. (**a**) A linear Yb:fiber oscillator and chirped-pulse amplifier [11, 130] (WDM—wavelength-division multiplexer; SBR—saturable Bragg reflector; FBG—fiber Bragg grating; PZT—piezo-electric transducer). This type of system can be used to produce (**b**) a tunable comb in the mid-IR with an optical parametric oscillator [68] (DM—dichroic mirror, PBS—polarizing beamsplitter, PD—photodetector, PCF—photonic crystal fiber, SC—supercontinuum), (**c**) a broadband comb in the visible and near-IR from nonlinear fiber [18], and (**d**) an XUV comb using cavity-enhanced high-harmonic generation [64]

For example, Fig. 8.2 shows how a high average power Yb:fiber comb has been used to generate frequency combs in different spectral ranges via various nonlinear processes: a comb in the mid-infrared with an optical parametric oscillator (OPO) [Fig. 8.2(b)] [68], a comb spanning over 1.5 octaves in the near-infrared by the use of a highly nonlinear fiber [Fig. 8.2(c)] [18], and a comb in the XUV down to 50 nm with high-harmonic generation [Fig. 8.2(d)] [64].

Er:Fiber Er:fiber lasers mode-locked (typically) using nonlinear polarization rotation [132, 133] have become very popular for several reasons. First, since they produce combs near 1550 nm, they can take advantage of telecommunication technology and are inexpensive and fairly easy to build. Second, they can be made entirely out of fiber, without any free-space sections, which makes them very robust and portable [134] as demonstrated in a drop tower experiment with a deceleration of 50 g [135]. It is also possible to split the comb output into multiple branches and amplify each branch separately without loss of coherence [136], thus providing a large amount of flexibility. With highly nonlinear fiber, Er:fiber lasers can cover a wavelength range from 1000 nm to over 2100 nm [56]. When combined with SHG, they can be used to provide tunable combs throughout the visible region [137]. They have also been used for mid-infrared comb generation using either DFG [138] or OPO [139]. However, the output power of amplified Er:fiber lasers is currently limited to typically 500 mW per branch. Also, their spectral coverage without broadening or frequency conversion is not ideal for spectroscopy. Repetition rates up to 1 GHz have been demonstrated [140], typically limited by the fiber length needed to obtain sufficient gain and compensate for dispersion.

Tm:Fiber and Cr:ZnSe Two newly developed mode-locked lasers have pushed the operating wavelengths toward the mid-infrared. Tm:fiber combs [75], which operate at 2 to 2.1 μm, function in many ways similarly to Yb:fiber lasers, sharing many of their advantages and disadvantages. Currently, they can provide about 1 W of power at repetition rates up to about 100 MHz, although there is no foreseeable reason that those could not be increased. Instead of directly mode-locking a Tm:fiber laser, it is also possible to seed a Tm:fiber amplifier with the spectrally shifted output of an Er:fiber comb [141]. The primary advantage of Tm:fiber systems is that they allow the use of new nonlinear crystals with transmission windows starting above 1.6 μm for frequency conversion farther to the mid-IR [70]. The second new system is a Cr:ZnSe mode-locked laser operating around 2.5 μm [91], which is similar in many aspects to Ti:sapphire lasers. The fractional gain bandwidth for Cr:ZnSe is even larger than that of Ti:sapphire, which provides the potential for ultrashort pulse generation in the mid-IR and thus a broad spectral bandwidth directly from the laser. Currently, however, challenges such as cavity-dispersion control [76] and stability have limited the use of Cr:ZnSe lasers.

DFG and OPO The most common approaches for producing mid-infrared frequency combs beyond 3 μm are either DFG or parametric generation (using an OPO). DFG combs have been demonstrated using the spectrum generated directly

from a Ti:sapphire laser [142]; however, the achievable powers are very low. More power can be obtained by using two synchronized Ti:sapphire lasers [143], but this is experimentally challenging. Multi-branch Er:fiber lasers enable mW-level tunable DFG: one branch is equipped with a nonlinear fiber to provide tunable frequency-shifted light and the second branch provides high-power, unshifted light [138, 144]. Up to 100 mW of DFG-based mid-IR light has recently been achieved using a fan-out periodically-poled crystal and a Yb:fiber laser [145]. In this case, some of the light from the fiber laser was sent through a nonlinear fiber and the red-shifted Raman soliton was mixed with the remaining unshifted pump light to generate the difference frequency. DFG systems are convenient and compact, but the power limitations can hinder some applications.

Higher power is possible with an OPO in which the signal and/or idler light produced by parametric generation is resonant with a cavity containing a nonlinear crystal. This greatly increases the conversion efficiency but also adds some complexity. For comb generation the cavity is pumped synchronously, i.e. the OPO cavity free spectral range matches an integer multiple of the pump-laser repetition rate. In addition, the cavity length must be actively controlled since it sets the f_0 of the generated comb [68, 146, 147]. Using a fan-out periodically-poled lithium niobate (PPLN) crystal, a comb has been demonstrated with a simultaneous bandwidth of up to 200 nm, a center wavelength tunable from 2.8 μm to 4.8 μm, and an output power up to 1.5 W at 136 MHz repetition rate [Fig. 8.2 (b)] [68]. It is also possible to construct an OPO with degenerate signal and idler frequencies (a "divide-by-two" system), which has been used to produce near-octave spanning spectral bandwidth around 3.3 μm [69, 148]. The long wavelength limit to the attainable spectral range is set by the absorption edge of the nonlinear crystals. To reach longer wavelengths crystals other than lithium niobate must be used. These are usually angled-tuned crystals such as $AgGaSe_2$ [149]. Recently, periodic patterning of GaAs has been developed, which could enable significantly higher OPO output powers. To use GaAs for mid-infrared generation, the pump wavelength must be above about 1.6 μm, thus the increased interest in Tm:fiber systems. Very recently, an octave-spanning mid-infrared spectrum covering up to 6.1 μm was demonstrated with a Tm:fiber laser and a degenerate OPO using orientation-patterned GaAs [70], although the average power was only about 30 mW.

8.3 Comb-Cavity Coupling

Efficient coupling of the frequency-comb light into a cavity is possible because the frequency-domain spectrum of Fabry-Perot cavity and that of an OFC are similar in structure. However, while the comb line spacing is constant, the optical cavity resonances are separated from each other by a frequency-dependent free spectral range (*FSR*) [150], given by

$$FSR(\omega_0) = \frac{c}{2L + c\frac{\delta\phi}{\delta\omega}|_{\omega_0}}, \tag{8.4}$$

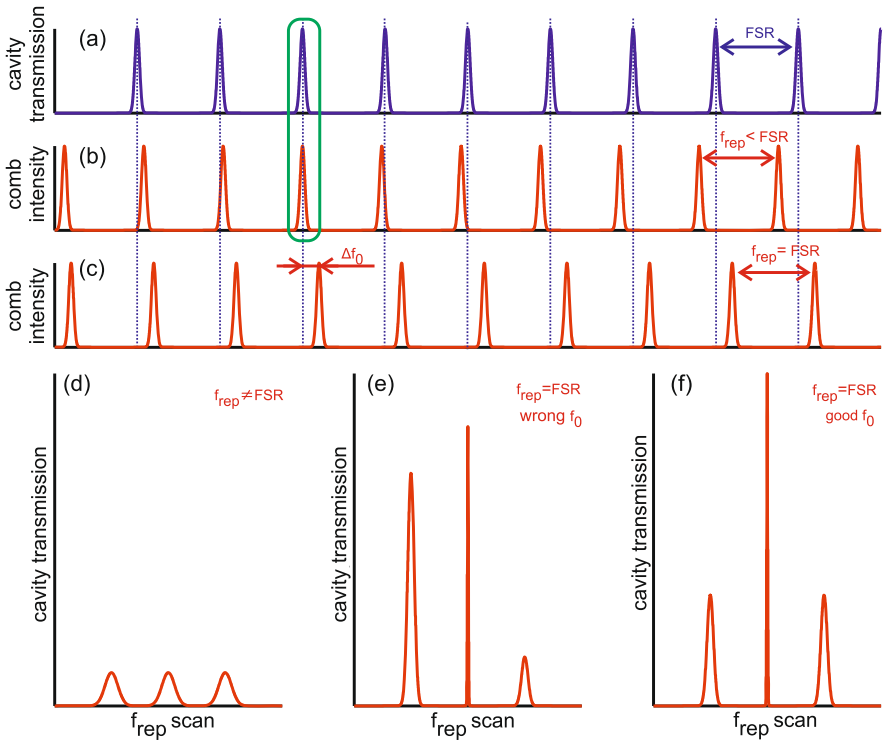

Fig. 8.3 Optimization of comb-cavity coupling. The optical cavity modes are shown in (**a**), the OFC spectrum with f_{rep} not matched to the cavity *FSR* in (**b**), and the comb spectrum with the correct f_{rep} but incorrect value of f_0 in (**c**). In (**d**)–(**f**), the cavity transmission signal during a scan of f_{rep} around different central values of f_{rep} and for different values of f_0 is presented. (**d**) As indicated by the common box in (**a**) and (**b**), even for $f_{\mathrm{rep}} \neq FSR$ there is coincidental overlap between some of the cavity and the OFC modes, resulting in low and broad transmission peaks. (**e**) When f_{rep} is scanned around the value matched to the *FSR* but the f_0 is not optimized, the heights of the two side peaks are asymmetric, while (**f**) when f_0 is correct the height of the main transmission peak is maximal and the heights of the two neighboring peaks are equal

where c is speed of light, L is the length of the cavity, and $\frac{\delta\phi}{\delta\omega}$ represents the intra-cavity dispersion, typically originating mostly from the cavity mirror coatings. This dispersion term means that the separation of consecutive cavity resonant modes is approximately constant only in a limited frequency range. Thus, some care must be taken to minimize the cavity dispersion at the spectral region of interest, usually by operating as close as possible to the maximum of the mirror reflectivity.

An analysis of the comb-cavity coupling [52] shows that optimum coupling requires matching both the spacing (set by f_{rep}) and absolute frequencies (f_0) of the comb lines with corresponding cavity modes over as wide spectral range as possible. This implies that the repetition rate of the OFC must be matched to the cavity *FSR* (or an integer multiple or sub-harmonic thereof) at the spectral region of interest. As shown in Figs. 8.3(a)–(b), an incorrect repetition rate results in an overall

mismatch between the comb lines and cavity resonances. Optimizing f_{rep} can be accomplished by changing the laser oscillator cavity length, for example with a piezo-electric transducer (PZT) that moves a mirror in the free-space part of the laser cavity (in a Ti:Sapphire or fiber lasers) or by stretching a piece of fiber in all-fiber laser sources [151]. Once the f_{rep} is matched to the cavity *FSR* as shown in Fig. 8.3(c), the f_0 of the comb also has to be chosen appropriately so that the resonances of the cavity and comb lines coincide, making the value of Δf_0 in Fig. 8.3(c) equal to zero. Tuning of f_0 is realized by modifying the dispersion of the laser cavity either by introducing an additional optical component such as a prism or by changing the power of the pump laser (which couples to the cavity dispersion through the nonlinear index of refraction of the gain medium) [5, 152].

The proper values of f_{rep} and f_0 can be determined while sweeping either the repetition rate of the laser or the length of the enhancement cavity and observing the cavity transmission signal, such as presented in Figs. 8.3(d)–(f). As the central value of f_{rep} is tuned close to the correct value, the intensity of the observed peaks increases and their width decreases [Figs. 8.3(d) to (e)], since more comb lines come on resonance with cavity modes simultaneously [44]. After f_{rep} is matched to the cavity *FSR*, the value of f_0 is optimized by comparing the height of the transmission peaks next to the most prominent peak. The correct value of f_0 is found when the height of the center peak is maximized and the two neighboring peaks have the same height [cf. Figs. 8.3(e) and (f)].

Once the f_{rep} and f_0 are optimized, these values must also be maintained over an extended period of time. This can be achieved in two different ways: by tightly locking the comb and cavity modes in order to ensure a constant transmission through the cavity, or by modulation of either one of the comb parameters or the cavity *FSR* so that laser light is periodically coupled into the laser cavity (the swept coupling scheme). Each of these schemes has advantages and limitations as explained below.

8.3.1 Comb-Cavity Coupling—Tight Locking Scheme

In the tight locking scheme the match between the comb modes and cavity resonances is actively maintained with feedback. The error signal for stabilization can be generated with the Pound-Drever-Hall (PDH) [153] method, the Hänsch-Couillaud method [154], or with a dither lock, where the comb modes are dithered around the cavity modes (or vice-versa) with amplitude smaller or comparable to the full width at half maximum (FWHM) cavity linewidth.

One way to achieve a tight lock is to stabilize the two degrees of freedom of the frequency comb to an external frequency reference and to implement a feedback loop that actively controls the cavity *FSR* to match it to f_{rep}. A difficulty arises due to the fact that for different cavity conditions (e.g. at different intra-cavity pressures) the optimum comb f_0 takes different values, so the locking electronics must be able

to follow these changes. Another limitation arises from the fact that the length of linear cavities is often controlled with a large-travel-range PZT. This, combined with the large mass of the cavity mirrors, results in a PZT response bandwidth usually limited to a few hundred Hz, which is not fast enough to remove high-frequency (acoustic) noise, although in principle this can be addressed by designing a cavity that can accommodate a lower-mass mirror.

An alternative scheme is to lock the comb to the resonances of the enhancement cavity by stabilizing the two degrees of freedom of the comb with two servo loops—one for f_{rep} and another for f_0. The error signals for each of the feedback loops are derived from different parts of the cavity reflection spectrum. This can be accomplished by applying a modified PDH detection scheme, using separate photodiodes to detect different parts of the reflected laser spectrum after diffraction from a grating. A detection scheme using three photodiodes was implemented in Ref. [152]: here the PDH error signal from the center of the reflected spectrum was used to control f_{rep} and the difference between two error signals from opposite ends of the reflection bandwidth was used to control f_0. A similar setup using only two error signals obtained in reflection was used in later experiments [45, 155] where an Er:fiber comb spanning from 1510 to 1610 nm was tightly locked to an enhancement cavity with a finesse of 8000. This enabled a 50-nm transmission bandwidth centered at 1530 nm, limited by the dispersion of the dielectric mirror coatings, which were designed for peak reflectivity at 1600 nm.

The two-point locking scheme was also used in the experiment shown in Fig. 8.4, where a mid-infrared OPO was tightly locked to a cavity with a peak finesse of 3800 at 3.8 μm and a Fourier-transform spectrometer was used for sensitive detection of C_2H_2, NO_2 and H_2O_2 [156]. A portion of the reflected beam from the cavity was dispersed with a diffraction grating, and two widely separated spectral regions were detected with two photodiodes, PD1 and PD2. The PDH error signal from PD1 was transformed by a proportional-integral (PI) filter with a corner frequency of 30 kHz and sent to a fast PZT controlling the length of the Yb:fiber pump-laser cavity, effectively changing f_{rep}. The output signal of the PI filter was further integrated and sent to a fiber stretcher in the Yb:fiber oscillator, cancelling low frequency drifts of the repetition rate. The second error signal, obtained from PD2, passed through a second PI filter with a corner frequency of 30 kHz and was sent to a fast PZT in the OPO cavity, effectively changing f_0 of the mid-IR comb [147, 157].

Figures 8.5(a) and 8.5(b) show the transmission spectra of the cavity measured with the Fourier-transform spectrometer at two different wavelength regions (solid blue curves). The locking points used by the f_{rep} and the f_0 feedback loops are marked in red and black, respectively. For comparison, the dashed blue lines show the transmission curves with only one locking point used (i.e., stabilizing only f_{rep} and with f_0 deliberately mismatched to reduce the transmitted bandwidth) as the locking point is tuned across the spectrum. As seen by comparison of the solid blue curve with the peaks of the dashed curves, the two-point locking enables broadband cavity-comb coupling with almost the entire incident OPO spectrum transmitted. In the wavelength region shown in panel (b) the losses on the edges of the

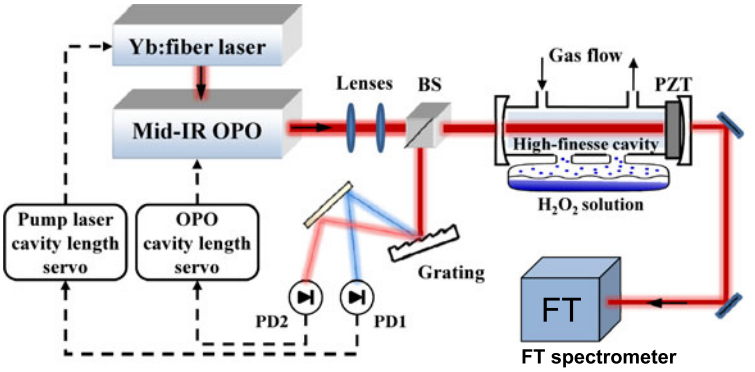

Fig. 8.4 Schematic of a CE-DFCS setup at 3.8 μm using two-point cavity locking. The optical parametric oscillator (OPO) is synchronously pumped by a femtosecond Yb:fiber laser and delivers an OFC tunable from 2.8 to 4.8 μm (see Fig. 8.2). The mid-IR comb is locked to a high-finesse cavity containing the gas sample by the use of a two-point tight locking scheme. In this scheme, the cavity reflected light is isolated with a beam splitter (BS) and sent onto a diffraction grating, which disperses the spectrum. Two distantly separated parts of the spectrum are measured on two photodetectors (PD1 and PD2) in order to create PDH error signals at the two wavelengths. The feedback signals are sent to the pump laser (mostly influencing f_{rep}) and the OPO cavity length (f_0). One mirror of the enhancement cavity is mounted on a PZT to allow adjustment of the cavity length. The light transmitted through the cavity is coupled into a fast-scanning Fourier-transform (FT) spectrometer (from Ref. [156]. With kind permission from Springer Science+Business Media: Appl. Phys. B, Cavity-enhanced optical frequency comb spectroscopy in the mid-infrared application to trace detection of hydrogen peroxide, vol. 110, year 2013, p. 163, A. Foltynowicz et al., Fig. 2a)

comb spectrum were more severe because of the larger mirror dispersion around 3900 nm [farther from the peak cavity finesse, plotted in Fig. 8.5(c)]. In particular, less light is coupled into the cavity at longer wavelengths (i.e., past 3950 nm) where the *FSR* of the cavity changes more rapidly. The larger dispersion also necessitated choosing the two locking points closer to each other. For this particular cavity, the transmission bandwidth with two-point locking ranged from 150 nm at 3700 nm to 70 nm at 3900 nm, which allowed simultaneous recording of the entire band of N_2O [Fig. 8.5(d)].

The two-point locking scheme enables broadband, tight locking of the comb modes to the cavity resonances, maximizing the enhancement factor and providing constant, high-power signal in cavity transmission. It can therefore be efficiently combined with Fourier-transform-based detection methods. On the other hand, this scheme requires more complicated locking electronics compared to the swept coupling scheme and also requires higher-bandwidth servo actuators in the laser systems. Moreover, residual frequency noise is translated into amplitude noise (FM-to-AM conversion) by the cavity resonances, which must be actively removed to reach high signal-to-noise ratio [155], as will be discussed later.

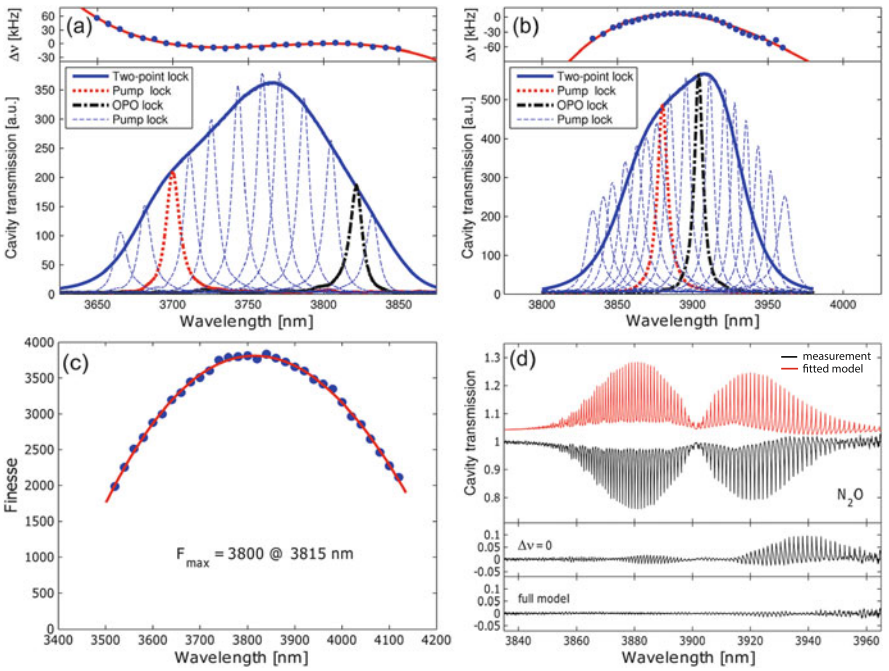

Fig. 8.5 Characterization of the two-point tight lock between a mid-IR comb and a cavity. (**a**) and (**b**) show the comb transmission through the cavity when both feedback loops are on (*solid blue*) for a center OPO wavelength of 3770 and 3920 nm, respectively. The two locking points are shown by the *red* (pump laser lock) and *black* (OPO lock) *dotted curves* when they are individually activated. The cavity transmission spectra with only one locking point tuned across the OPO spectrum are shown as *dashed blue curves*. The frequency mismatch between cavity and comb modes ($\Delta\nu$) when both loops are on is shown in the *upper part of the panels*. (**c**) The wavelength-dependent finesse of the cavity. (**d**) The spectrum of 0.8 ppm of nitrous oxide at the pressure of 760 Torr of nitrogen at room temperature recorded in 1 s (*black*) and the fitted model spectrum (*red*). The *lower parts* of (**d**) show fit residuals using two models, the first one ignoring the mismatch between comb modes and cavity modes and the second one based on the full model of Eq. (8.5), which improves the fit significantly (from Ref. [156]. With kind permission from Springer Science+Business Media: Appl. Phys. B, Cavity-enhanced optical frequency comb spectroscopy in the mid-infrared application to trace detection of hydrogen peroxide, vol. 110, year 2013, p. 163, A. Foltynowicz et al., Figs. 3, 4, 5)

8.3.2 Comb-Cavity Coupling—Swept Coupling Scheme

The walk-off between the comb lines and the cavity modes due to dispersion in the mirror coatings is the main factor limiting the spectral bandwidth that can be achieved for most CE-DFCS experiments with the tight comb-cavity lock. Moreover, the bandwidth limitation is more severe when a higher finesse cavity is used, resulting in a compromise between the sensitivity enhancement factor and the simultaneously usable spectral bandwidth. The negative effects caused by cavity dispersion can be reduced by special low-dispersion cavity designs (including prism

cavities based on total internal reflection) [158]. Alternatively, the swept coupling scheme allows the entire spectral bandwidth of a comb to be transmitted through the cavity, as demonstrated both in early applications of ML-CEAS [51] as well as in CE-DFCS experiments [43]. In this scheme, the comb modes are periodically swept across the cavity modes (or vice versa) with the amplitude of the sweep larger than the FWHM linewidth of the cavity resonance (in contrast to dither lock), resulting in periodic transmission peaks. By stabilizing the time interval between the transmission peaks (with feedback to either the comb or the cavity), it is possible to eliminate slow drifts between the cavity and comb modes. The dispersion problem is largely avoided as the corresponding mode pairs come into resonance rapidly one after another, thus when averaging over a sweep, the full bandwidth of the source spectrum is transmitted [43]. In addition, the bandwidth required of the locking electronics is much lower than in the tight locking scheme, since low-bandwidth feedback is sufficient to stabilize the time between transmission peaks. Another advantage is that the swept coupling scheme efficiently reduces amplitude noise in cavity transmission caused by low-frequency mechanical noise and by cavity FM-to-AM noise conversion.

The main disadvantage of this method is the reduction of the useful experimental duty cycle and transmitted power arising from the limited time over which the comb modes are on resonance with the cavity. A more subtle effect is connected with the enhancement factor of the absorption signal. The enhancement of the interaction length is related to the cavity finesse, F, which is proportional to the inverse of the cavity losses. For fast sweeps, the time that the comb lines spend on resonance becomes only a fraction of the cavity lifetime. This results in an enhancement factor that is closer to F/π for rapid sweeps instead of $2F/\pi$ for the tight locking case [43, 55], which decreases the absorption sensitivity assuming the same fractional noise levels. The fact that the enhancement factor is dependent on the sweep parameters implies that a calibration of the effective length enhancement can be necessary for intermediate sweep speeds, although this is not absolutely necessary for higher sweep speeds as the enhancement factor approaches F/π. While the swept coupling scheme can be combined with Fourier-transform-based detection methods, the performance is worse than with a tight lock [159], due to the fact that the amplitude modulation of the transmission signal leads to a disturbance of the detected interference signals.

The swept cavity-comb coupling scheme has been used in ML-CEAS and CE-DFCS multiple times [44, 51, 57], and its robustness and reliability has been demonstrated by its application for trace gas detection in the north coast of France [55, 160] and in the Antarctic [161]. Amplitude noise reduction down to the shot-noise level has also been demonstrated [162].

An example of an experimental setup using the swept coupling scheme and a VIPA spectrometer (Sect. 8.4.2) is shown in Fig. 8.6. The FSR of the enhancement cavity, with a finesse of 28000, was matched to the f_{rep} of the Er:fiber comb. To couple the frequency comb to the cavity, the positions of the frequency comb lines were modulated with respect to the cavity resonances at a frequency of 1.5 kHz by sweeping f_{rep}. The sweep amplitude was chosen such that the comb lines were on

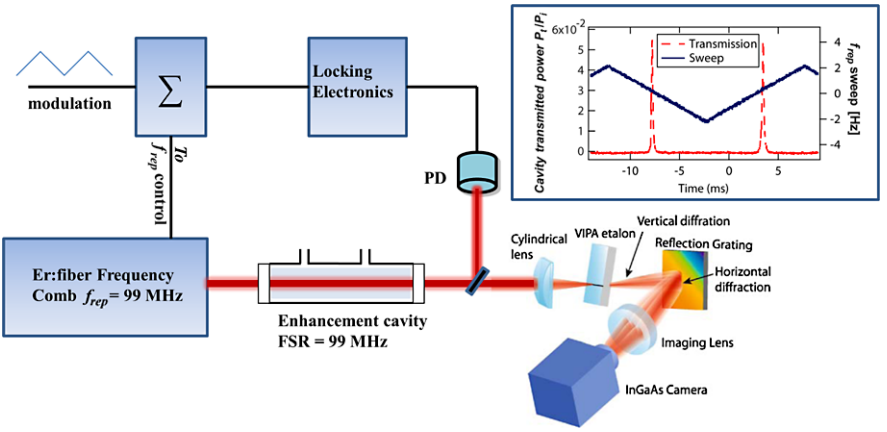

Fig. 8.6 Schematic of a CE-DFCS experimental setup with swept coupling scheme working in the 1.5–1.7 μm range. The repetition rate of the Er:fiber frequency comb was modulated, and a small part of the light transmitted through the cavity was focused on a photodetector (PD), whose output signal was used to generate the feedback signal applied to the f_{rep} control of the Er:fiber frequency comb ($\sum$—summing box). The *framed inset* shows the PD signal for a 100 nm incident spectrum while f_{rep} is scanned. The light transmitted through the cavity was analyzed with a VIPA spectrometer [43]

resonance with the cavity for 1/3 of the modulation period. The inset in Fig. 8.6 shows the cavity transmission measured by the photodetector in front of the VIPA spectrometer when f_{rep} was swept with a larger amplitude. Due to low cavity dispersion and optimized cavity-comb coupling, the cavity transmission signal on the photodiode was sharply peaked. The time between the successive transmission signals was used to produce an error signal. This error signal, after integration, was fed back to the laser repetition rate control, which allowed stable, long-term operation and transmission of the entire laser bandwidth through the cavity [43].

8.3.3 *Effect of Comb-Cavity Resonance Mismatch on the Observed Line Shape*

In the tight locking scheme, the centers of the cavity and comb modes are not perfectly matched over the entire transmission bandwidth, as shown in the upper panels of Figs. 8.5(a) and (b). This mismatch causes a distortion of the line shapes in the observed absorption spectrum, which can be seen in Fig. 8.5(d). This effect, visible in numerous experiments, must be taken into account in the data analysis to accurately determine the molecular concentrations.

The intensity of a single comb line at a frequency ν transmitted through a cavity containing an absorbing sample is given by [155, 156]

$$I_t(\nu) = I_0(\nu)\frac{t^2(\nu)e^{-2\delta(\nu)L}}{1 + r^2(\nu)e^{-4\delta(\nu)L} - 2r(\nu)e^{-2\delta(\nu)L}\cos[2\phi(\nu)L + \varphi(\nu)]}, \tag{8.5}$$

where $I_0(\nu)$ is the intensity of the comb line incident on the cavity, $t(\nu)$ and $r(\nu)$ are the frequency-dependent intensity transmission and reflection coefficients of the cavity mirrors, respectively, $\delta(\nu)$ and $\phi(\nu)$ are the attenuation and phase shift of the electric field per unit length due to the analyte, and $\varphi(\nu)$ is the round-trip phase shift in the cavity, given by $4\pi\nu nL/c$, where n is the refractive index of the buffer gas. If there is a mismatch of $\Delta\nu$ between a comb mode and the center of the nearest cavity mode, the round-trip intra-cavity phase shift is equal to $\varphi(\Delta\nu) = 2q\pi + 2\pi\Delta\nu/FSR$, where q is an integer mode number. At frequencies close to molecular transitions, the molecular dispersion adds an additional shift to the cavity modes. This results in the characteristic overshoots observed in the absorption line shapes, easily visible in the upper fit residuals in Fig. 8.5(d). In addition to the lineshape asymmetry, the peak absorption is reduced, which can lead to underestimation of the molecular concentrations. The model of Eq. (8.5), when applied to data in Fig. 8.5(d), is able to significantly decrease the discrepancies between the measured and theoretical spectra, as presented in the bottom fit residuals in Fig. 8.5(d).

8.4 Detection Methods

The frequency comb light transmitted through the enhancement cavity contains broadband spectroscopic information about the interrogated system; however, this broadband information must be detected to be of use. In some DFCS measurements, a single atomic or molecular transition, well separated from other spectroscopic features, served as an optical frequency discriminator by only interacting with a single comb tooth (e.g., [64]), removing the need for a broadband, parallel acquisition system. For sensing applications with dense spectra, the capability to make simultaneous measurements across tens of thousands of parallel channels with high spectral resolution is required. Thus the applied detection techniques have to satisfy two seemingly contradicting requirements—broadband operation and high spectral resolution—while also providing high sensitivity for absorption. Although the perfect experimental setup with unlimited spectral bandwidth and resolution does not exist, several detection schemes allowing multiplexed acquisition have been demonstrated and are summarized in Fig. 8.7.

In the initial work on ML-CEAS, the output of the enhancement cavity was dispersed with a grating spectrograph and detected with a detector array [Fig. 8.7(a)], and the FM-to-AM noise conversion due to the cavity was circumvented with the swept coupling scheme (Sect. 8.3.2) [51]. The sensitivity was increased in later experiments with active feedback to the cavity length and by using higher finesse

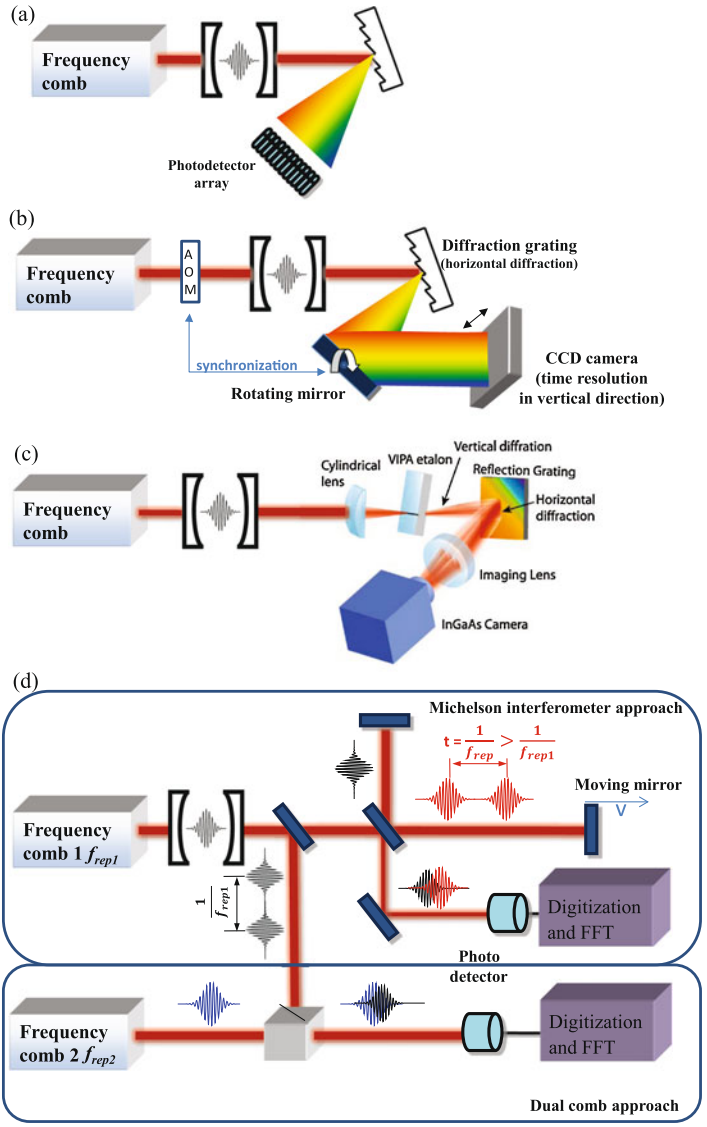

Fig. 8.7 Detection schemes for CE-DFCS. (**a**) A grating spectrometer equipped with a detector array. (**b**) Broadband cavity ringdown setup. A grating provides spectral dispersion in the horizontal direction and a rotating mirror creates the time scale in the vertical direction for a two-dimensional detector array. An acousto-optic modulator (AOM) is used to turn off the laser beam to initiate the ringdown. (**c**) A VIPA spectrometer. The cavity output is dispersed vertically with a high-resolution VIPA etalon and is cross-dispersed with a diffraction grating. (**d**) Femtosecond Fourier-transform spectrometer. In the Michelson interferometer approach, the cavity output is analyzed by an interferometer with a fast scanning mirror in one or both arms. This effectively changes the repetition rate of the OFC. The pulses of the combs from the two interferometer arms with different f_{rep} interfere on the detector. In the dual comb approach, the output of the enhancement cavity beats with another OFC with $f_{\mathrm{rep2}} \neq f_{\mathrm{rep1}}$ on a photodetector

cavities [54, 55], eventually reaching shot-noise limited performance [162]. This method, especially in combination with the swept coupling scheme, is fast and reliable and does not require any complicated locking schemes; however, due to the coupling scheme used, the transmitted power is significantly reduced thus reducing the shot-noise limited sensitivity. On the other hand, it is difficult to use this detection method with tight locking due to amplitude noise on the transmitted light. Also, the spectral resolution is limited by the grating spectrometer (typically to 10 GHz or above), which usually does not allow single comb modes to be resolved.

One way to avoid the FM-to-AM noise conversion introduced by the high-finesse cavity is to detect cavity-ringdown signals [Fig. 8.7(b), see Sect. 8.4.1], which are inherently more immune to intensity noise. To combine cavity-ringdown with CE-DFCS a two-dimensional detector is used [53]: one axis of the detector corresponds to time and the other corresponds to wavelength. The wavelength dispersion is obtained with a diffraction grating, resulting in the same limited spectral resolution. The temporal axis is generated with a rotating mirror to deflect the dispersed light or by clocking the readout of a CCD camera. The small number of resolved spectral elements, limited by the size of the detector array, has reduced the applicability of this readout method.

Higher spectral resolution and more spectral elements can be obtained with a virtually-imaged phased array (VIPA) etalon [163] combined with a grating cross-disperser and a two-dimensional detector array—schematically shown in Fig. 8.7(c) (Sect. 8.4.2). The resolution of a VIPA-based spectrometer can be 1 GHz or below, which can enable single-comb mode resolution [58, 145, 164]. As in the one-dimensional system, it is difficult to use tight locking due to FM-to-AM noise conversion; however, in combination with the swept coupling scheme [43, 44], this method provides high-resolution spectra with high sensitivity [57, 58].

It is also possible to employ Fourier-transform spectroscopy (FTS) techniques with CE-DFCS [Fig. 8.7(d)]. These spectrometers are based either on a Michelson interferometer with a mechanical translation stage [165] (Sect. 8.4.3) or dual comb spectroscopy [166, 167]. They allow measurements in the spectral range where a VIPA etalon is not readily available and also do not suffer from the trade-off between resolution and bandwidth due to the limited detector array sizes [168]. To deliver a good performance, FTS requires a continuous transmission signal and thus a tight comb-cavity lock. This can lead to increased amplitude noise if the comb modes are not stabilized to better than a small fraction of cavity resonance linewidth. An efficient scheme to circumvent this problem employing active cancelation of amplitude noise down to the quantum limit has recently been demonstrated [155] and provides long-term, uninterrupted operation. Commercial FTIRs have been used with the swept-coupling scheme as well, but this combination tends to result in decreased absorption sensitivity and lower quality of spectra [159, 169].

Another way to avoid the frequency resolution limitation of a grating spectrograph is to use a Vernier spectrometer [170], in which the cavity *FSR* is purposefully mismatched from the comb f_{rep} so that the cavity only transmits comb teeth separated by kf_{rep} (k is an integer depending on the *FSR*). This is illustrated in Figs. 8.8(a)–(b) for the specific case where the cavity *FSR* is equal to $4f_{\mathrm{rep}}/5$. As

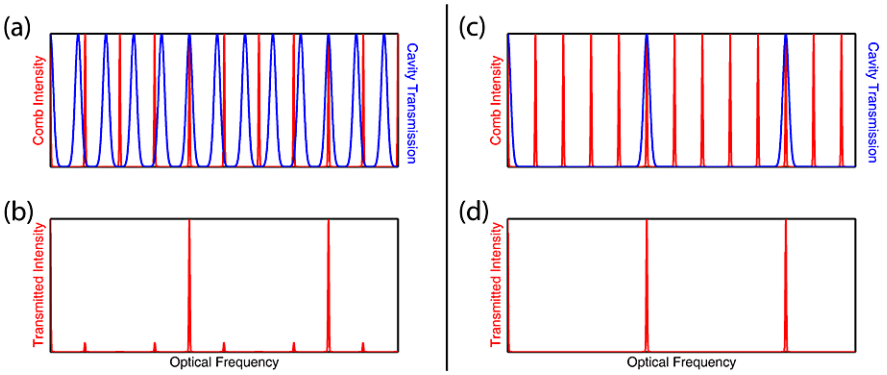

Fig. 8.8 Comb filtering using Vernier spectroscopy or a filter cavity. (**a**) Cavity transmission spectrum (*blue*) with $FSR = 200$ MHz and spectrum of an OFC (*red*) with repetition rate of 250 MHz ($FSR/f_{\mathrm{rep}} = 4/5$), (**b**) transmitted comb spectrum (*red*) in which the comb spacing, effectively quadrupled, equals to $4f_{\mathrm{rep}} = 1000$ MHz. The residual transmission between the main peaks is largely suppressed. (**c**–**d**) Cavity filtering by setting $FSR = 4f_{\mathrm{rep}}$. The transmitted comb spectrum (**d**) again has spacing equal to 1000 MHz

a result, in the frequency domain, the separation of the transmitted comb teeth is increased by a factor of four; with a different cavity length the separation could be significantly higher. A similar result can be obtained using a filter cavity with $FSR = 4f_{\mathrm{rep}}$ to filter the comb, as shown in Figs. 8.8(c)–(d). In this way, it is possible to increase the separation of the transmitted comb teeth to be resolvable by the grating. Thus an experimental setup similar to the one illustrated in Fig. 8.7(a) can be used, with a detector array recording a single comb line on each pixel. However, a major drawback is that due to the filtering effect more scanning is required to record a full spectrum. In addition, the swept-coupling scheme is challenging to use with the Vernier scheme, while with the filter cavity approach, the interaction length with the sample is significantly decreased (due to the shorter cavity length) or two cavities are required. The approach of comb filtering has found application in calibration of astronomical spectrographs with the frequency comb, where a mode spacing of tens of GHz is desired [171–173].

8.4.1 Broadband Cavity Ringdown Spectroscopy

In cavity ringdown spectroscopy (CRDS) [174], the decay rate of the light leaking out of the enhancement cavity is measured after removal of the input light; thus it is less sensitive to intrinsic intensity noise caused by FM-to-AM noise conversion. Unfortunately, multichannel detectors typically only offer readout rates from Hz to tens-of-kHz, depending on the size of the detectors, which is too slow for broadband CRDS. This problem was circumvented with an approach called broadband ring-down spectral photography [175, 176] where a rotating mirror was used

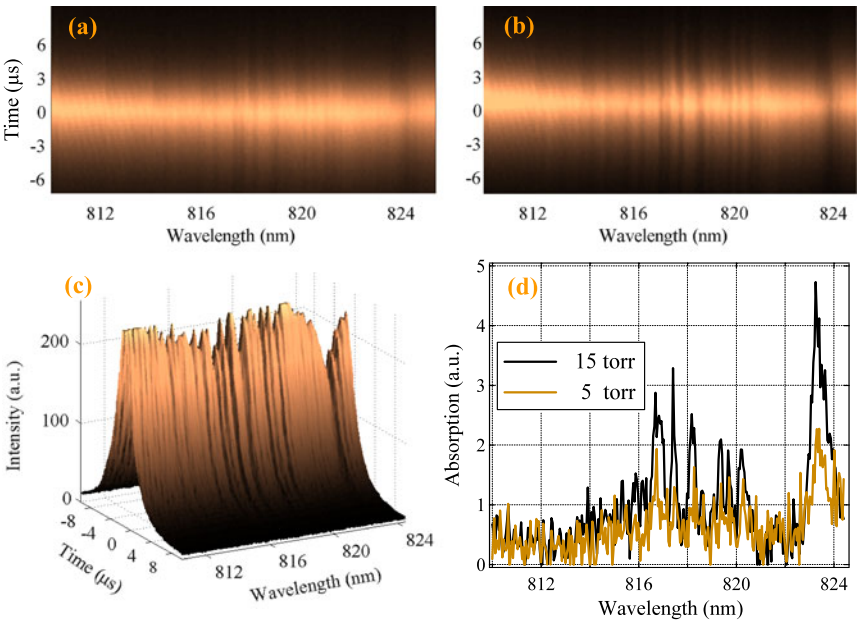

Fig. 8.9 Results from broadband CRDS. (**a**) and (**b**) Images of broadband ringdown spectra of the H_2O overtone spectrum at pressures of 5 and 15 Torr, respectively, acquired in 30 μs. In (**c**) a surface plot of 15 averaged images is plotted, showing the lower buildup power and faster decays in spectral regions containing H_2O absorption lines. (**d**) The resulting spectra of H_2O at pressures of 15 and 5 Torr (from Ref. [53]. Reprinted with permission from AAAS)

to create time axis in the plane of a two-dimensional camera. A similar result was achieved with no moving parts by clocking the readout of a CCD array [177]. CRDS was for the first time applied to measurements with an optical frequency comb in Ref. [53]. The experimental setup, shown schematically in Fig. 8.7(b), was based on a Ti:sapphire frequency comb centered at 800 nm, which allowed access to overtone spectra of C_2H_2, H_2O, NH_3, and forbidden electronic transitions of O_2. The comb light was coupled to an enhancement cavity with a finesse of 4500. The cavity output was dispersed horizontally by a grating and focused at the imaging plane of a 2D camera. A rotating mirror placed between the imaging lens and the camera moved the beam vertically along the detector array for temporal resolution. An AOM in front of the the cavity was used to rapidly switch off the comb light and start the decay event. The resulting images are presented in Fig. 8.9. The system allowed simultaneous measurement of 340 ringdown events with 25 GHz spectral resolution, reaching an absorption sensitivity of 2.5×10^{-10} cm^{-1} Hz$^{-1/2}$. A typical ringdown spectrum covering a 15 nm bandwidth was acquired in 30 μs.

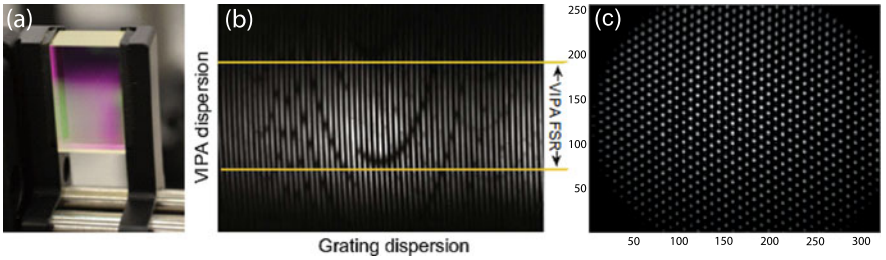

Fig. 8.10 (**a**) Virtually-imaged phased array (VIPA) etalon. The brighter stripe in the lower part is the entrance slit. (**b**) An image from a VIPA spectrometer working around 1600 nm. *Dark spots* indicate CO_2 absorption features; *yellow lines* indicate one VIPA *FSR*, which is the area with unique spectral information (from Ref. [43]). (**c**) The comb-mode resolved image from a VIPA spectrometer at 3800 nm. The separation between the comb lines is 2 GHz (obtained by cavity filtration of a lower repetition rate comb); the single OFC modes are clearly resolved (from Ref. [145])

8.4.2 VIPA Spectrometer

A VIPA, or virtually-imaged phased array [163, 178, 179], is a rectangular etalon plate [Fig. 8.10(a)] with a high reflectivity coating on the entrance surface (reflectivity >99.9 %) and a lower reflectivity back surface (reflectivity typically about 97 %). Additionally, an antireflection-coated entrance stripe is placed at the bottom of the entrance surface [visible in Fig. 8.10(a)] to allow light, which is focused in one dimension, to be coupled into the device. In contrast to an ordinary Fabry-Perot etalon, the VIPA etalon is tilted at an angle; because of this and the focusing of the incoming light, it transmits all the incident wavelengths. At the output it generates a pattern of overlapping mode orders that repeat at the etalon *FSR*—typically 50 to 100 GHz, depending on the thickness of the plate. The main advantage of a VIPA is the extremely high angular dispersion, up to 30–40 times higher than a traditional (first-order) diffraction grating. To spectrally resolve overlapped orders a cross-dispersion grating with a resolution better than the VIPA *FSR* is used. After the grating the light is imaged on a two-dimensional camera.

An example of the resulting image is shown in Fig. 8.10(b). The vertical stripes are single mode orders of the VIPA, which are dispersed in the horizontal direction by the lower-resolution grating. The yellow horizontal lines show the range of one VIPA *FSR* on the camera, where the spectral information is unique. Thus, a single column within this region contains spectral information from one VIPA *FSR*. By reading the pixels column-by-column a traditional one-dimensional spectrum can be created. The dark spots in the image represent CO_2 absorption signals for individual ro-vibrational transitions around 1600 nm.

The resolution of the VIPA spectrometer is limited by the finesse and *FSR* of the etalon. The finesse is determined both by the reflectivity of the coatings and by the number of round-trip passages within the tilted etalon. Resolution of 500 MHz has been demonstrated with VIPA *FSR*s of 25 to 100 GHz. This is sufficient to resolve single modes of high repetition rate combs, as demonstrated with Ti:sapphire combs

[58, 164]. Another approach to achieve comb mode resolution with lower repetition rate lasers is to use an intermediate filter cavity. This is shown in Fig. 8.10(c) for a filtered comb with 2 GHz mode spacing; here, the filter cavity was set to transmit every 15th comb tooth of a femtosecond mid-infrared OPO [145].

One advantage of VIPA spectrometers is the short integration time for a single image, on the order of tens to hundreds of μs [145], making them an ideal tool for studies of transient events. The fact that the setup does not involve any moving parts and is compact makes this technique particularly attractive for field-deployable devices. In addition, the approach is compatible with the swept coupling scheme, which reduces the overall complexity of the experimental setup. On the other hand, since the VIPA is an etalon the resulting fringe pattern is sensitive to optical alignment and to mechanical vibrations. Furthermore, calibration of the frequency axis needs to be carefully checked since the pixel-to-frequency mapping is nonlinear. VIPA etalons tend to be relatively expensive and are available only in limited spectral regions (a single etalon typically covers about 200 nm in the visible to near-IR ranges). Recently, a VIPA covering more than 1 μm in the important mid-IR region around 4 μm has been demonstrated [145].

8.4.3 Fourier-Transform Spectroscopy

Fourier-transform spectroscopy (FTS) based on interferometry with an incoherent light source is a workhorse for analytical chemistry and molecular science, providing broad bandwidth and relatively high spectral resolution [180]. It utilizes extremely broadband light sources between 2 and 50000 cm^{-1} and can reach resolutions of about 0.001 cm^{-1} (30 MHz, although resolutions of 1–10 GHz are more typical). The main shortcoming of this method is the long acquisition time, associated with the use of thermal light sources and the need for long averaging times to obtain high sensitivity. The lack of spatial and spectral coherence of thermal sources makes it very challenging to use long optical path length (required for high resolution) or to efficiently couple light into an enhancement cavity for high sensitivity [181].

Replacing the thermal source of an existing Fourier-transform (FT) spectrometer with an optical frequency comb offers an instantaneous increase in spectral brightness and thus reduces averaging times significantly. The coherent frequency comb also allows an efficient combination of cavity-enhanced spectroscopy and FTS. The schematic of a Michelson interferometer-based CE-DFCS setup is shown in Fig. 8.7(d): the comb is split in two arms of the Michelson interferometer with one arm scanning at a speed v (in practice both arms can be scanned simultaneously in opposite directions). The resulting time-domain interference signal is monitored by photodetectors at an output port of the interferometer. This interferogram is then Fourier transformed to obtain the frequency-domain spectrum, as in traditional FTS. When the spectrometer is capable of resolving each OFC mode, the actual resolution of each of spectral element is given by the comb-mode linewidth. This value is much

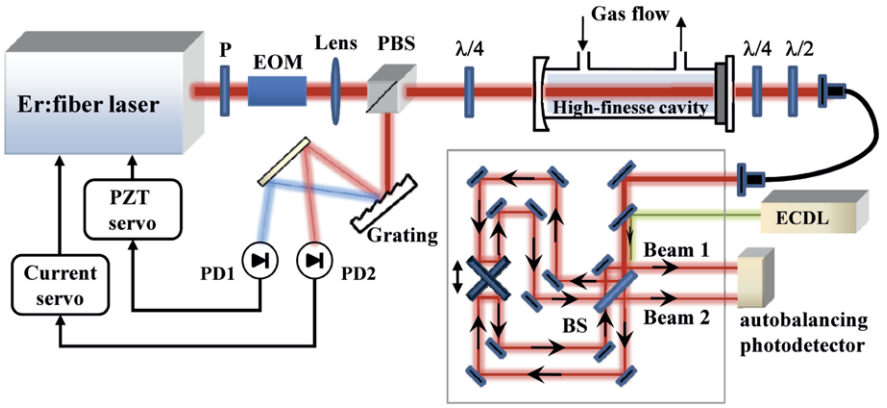

Fig. 8.11 Experimental setup for CE-DFCS near 1550 nm with FTS-based readout. An Er:fiber femtosecond laser is tightly locked to a high-finesse optical cavity containing a gas sample using a two-point PDH lock. An electro-optic modulator (EOM) is used to phase modulate the comb light at 14 MHz, and the cavity reflected light is dispersed by a grating and measured with two photodetectors (PD1 and PD2) in order to create error signals at two different wavelengths. The feedback is sent to the pump diode current controller and to a PZT inside the laser cavity. The cavity transmitted light is coupled through a polarization-maintaining fiber into a fast-scanning Fourier-transform spectrometer. The two outputs of the interferometer (beams 1 and 2) are incident on two photodiodes of an auto-balanced photodetector. The beam of a cw 780 nm external cavity diode laser (ECDL), used for frequency calibration, co-propagates with the frequency comb beam and is monitored with a separate detector (not shown). P—polarizer, (P)BS—(polarizing) beam splitter, $\lambda/4$—quarter wave plate, $\lambda/2$—half wave plate (from Ref. [155]. Reprinted figure with permission from A. Foltynowicz et al., Phys. Rev. Lett. 107, 233002. Copyright (2011) by the American Physical Society)

lower than the OFC mode spacing and improves on the resolution of traditional FTS setups by many orders of magnitude [182].

Michelson interferometer-based FTS has been applied as a detection method for DFCS [48, 67, 165, 183] as well as for CE-DFCS, either with a tight lock between the cavity and optical frequency comb [45, 155, 156] or with a swept coupling scheme [159, 169, 184, 185]. Figure 8.11 shows an FTS-based CE-DFCS system developed at JILA using a 250-MHz Er:fiber comb covering from 1510 to 1610 nm. The laser was locked to a 60-cm long enhancement cavity with a finesse of 8000 using the two-point locking scheme described in Sect. 8.3.1. The wavelengths for the locking points were chosen to assure high cavity transmission in the spectral range where strong acetylene absorption occurs (1530–1540 nm). The output light from the cavity was sent into a Michelson interferometer equipped with a fast-scanning delay stage on which two retro-reflectors were mounted. To increase the optical path difference corresponding to the movement of this stage, the lengths of both interferometer arms were scanned simultaneously but in opposite directions (Fig. 8.11). Light from a stable 780-nm cw laser co-propagated with the comb light and was used as a reference for frequency calibration. The comb interferograms at both output ports of the Michelson interferometer were monitored with an auto-balanced In-

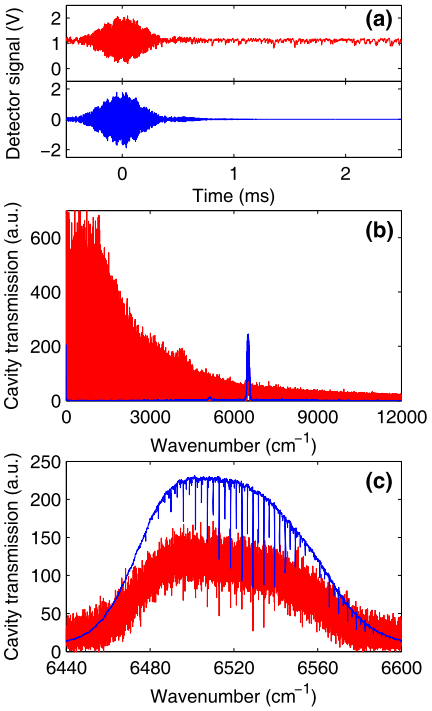

Fig. 8.12 Signals recorded by an FTS-based CE-DFCS setup. (**a**) Time-domain interferogram with auto-balanced detection disabled (*red*) and enabled (*blue*). (**b**) Frequency-domain signals with auto-balanced detection disabled and enabled (*red* and *blue*, respectively), with an expanded viewed of the region of interest, revealing acetylene absorption, in (**c**) (from Ref. [155]. Reprinted figure with permission from A. Foltynowicz et al., Phys. Rev. Lett. 107, 233002. Copyright (2011) by the American Physical Society)

GaAs detector [186], which subtracts the photo-currents from the two photodiodes and uses active feedback to keep the DC currents equal. This subtraction doubles the useful signal compared to a single interferometer output (due to the fact that the two output signals of the interferometer are complementary [187]) while removing common mode amplitude noise, mainly caused by FM-to-AM conversion by the enhancement cavity. Both interferograms (from the comb and the reference cw laser) were digitized by a two-channel analog-to-digital converter at 1 Msample/s with 22-bit amplitude resolution.

Figure 8.12 shows two time-domain interferograms and the resulting spectrum of acetylene recorded with this system. The signal obtained with one output of the interferometer blocked (corresponding to a single detector setup) is shown in red in panel (a), while the blue trace shows the signal recorded using the auto-balanced detection. Significant removal of amplitude noise is clearly visible, especially in the baseline at times greater than 1 ms. The use of auto-balanced detection decreased the noise at the interferogram fringe frequency (corresponding to 6500 cm^{-1}) by a factor of 600, down to the shot noise limit, significantly increasing the signal-to-noise ratio of the resulting spectrum, as shown in panels (b) and (c). The acquisition time of one scan with a spectral resolution of 380 MHz was 3 s and a shot-noise limited sensitivity of 1.4×10^{-9} cm^{-1} was obtained in the normalized spectrum, corresponding to 3.4×10^{-11} cm^{-1} Hz$^{-1/2}$ per spectral element.

In general the repetition rate of the pulse train reflected from a moving mirror in a Michelson interferometer arm is Doppler shifted in comparison to the ini-

tial repetition rate of the femtosecond laser. Therefore, the interference at the output port can be seen as that between two frequency combs with slightly different repetition rates ($\Delta f_{\mathrm{rep}} = 2\frac{v}{c} f_{\mathrm{rep}}$). This makes it equivalent to the dual-comb spectroscopy technique initially proposed in Ref. [166] and demonstrated by several groups [49, 65, 167, 168, 188, 189]. In this technique the heterodyne beat note between two frequency combs with different repetition rates creates an interferogram in the time domain [see Fig. 8.7(d)—dual comb approach box]. In most implementations of the dual comb technique, Δf_{rep} is set in the 0.2–4 kHz range, which assures short acquisition times of a single interferogram. Since the dual comb technique does not use any mechanical moving parts and the footprint of the detection system is compact, it is potentially suitable for field applications; however, the need for two fully stabilized femtosecond sources (as the performance depends strongly on the stability of the mismatch of the repetition frequencies) significantly increases the cost and complexity of the system. Referencing schemes using cw lasers have recently been demonstrated [190–192], which can lead to a relaxation of the requirements for repetition rate stabilities.

8.4.4 Sensitivity of CE-DFCS Detection Methods

The sensitivity of a detection system can be determined from the relative noise, σ, on the baseline of the spectrum. The minimum detectable absorption coefficient can be defined as

$$\alpha_{\mathrm{min}} = [\sigma / L_{\mathrm{eff}}] \left[\mathrm{cm}^{-1}\right], \tag{8.6}$$

where L_{eff} is the effective interaction path length with the sample. For a tight comb-cavity lock, L_{eff} is equal to $2FL/\pi$, where L is the physical cavity length (assuming a linear cavity); in the case of cavity ringdown, L_{eff} is reduced to FL/π. In intermediate cases, i.e., for the swept coupling scheme, L_{eff} takes a value between those two limiting cases [43]. When the system is white noise limited, α_{min} averages down with the square root of the number of samples, so the minimum detectable absorption coefficient normalized to 1-s acquisition time is used for comparison between systems:

$$\alpha_{\mathrm{min}}^{1\,\mathrm{s}} = [\sigma / L_{\mathrm{eff}}]\sqrt{T} \left[\mathrm{cm}^{-1}\,\mathrm{Hz}^{-1/2}\right], \tag{8.7}$$

where T is the acquisition time of the spectrum. Note that this formula is valid only if the system is white-noise limited on the time scale of a second or longer. For broadband systems such as DFCS, a figure-of-merit including the number of simultaneously resolved spectral elements, M, can be used. This absorption sensitivity per spectral element, $\alpha_{\mathrm{min}}^{\mathrm{DFCS}}$, is defined as

$$\alpha_{\mathrm{min}}^{\mathrm{DFCS}} = [\sigma / L_{\mathrm{eff}}]\frac{\sqrt{T}}{\sqrt{M}} \left[\mathrm{cm}^{-1}\,\mathrm{Hz}^{-1/2}\right]. \tag{8.8}$$

This value can be interpreted as the performance in terms of absorption sensitivity that a cw-laser system would need, including scanning time, to match the performance of the broadband system.

8.5 Applications

The powerful features of CE-DFCS make the technique attractive for numerous scientific applications. While a number of proof-of-principle experiments demonstrating the general capabilities of the technique have been reported, the list of systems applied to specific scientific problems is still relatively short [26, 48, 55, 57–60, 156, 160, 161]. A few of these are described in several extensive reviews [43, 44, 193]. In this section we present five systems developed at JILA with specific applications in mind and operating in different spectral regions spanning from the visible to the mid-IR. Combined they demonstrate the potential of applying CE-DFCS to a wide range of scientific fields. The first three examples illustrate broadband and ultra-sensitive detection of multiple molecular species using enhancement cavities: breath analysis using a VIPA spectrometer at 1.6 μm; semiconductor manufacturing gas impurity analysis with a broadband VIPA spectrometer at 1.75–2 μm; detection of hydrogen peroxide for medical applications using comb-FTS working at 3.74 μm. Two final examples show how resolving individual comb modes enables ultrahigh resolution with many simultaneous detection channels over a broad spectral bandwidth, which can then be used for rapid spectroscopy of cooled molecular beams and for velocity-modulation spectroscopy of molecular ions.

8.5.1 Breath Analysis

The idea of disease diagnosis based on the 'smell' of human breath can be traced back to Hippocrates. It has an enormous potential as a noninvasive, inherently-safe and low-cost method for disease detection, preventive medicine, and metabolic status monitoring. However, despite some progress, breath analysis is still not an established diagnosis tool, with the exceptions of NO detection (for asthma), and to some extent CO detection and $^{13}C/^{12}C$ ratio measurements, which have been used in a few clinical applications. A main issue preventing breath analysis from becoming a widespread diagnostic tool is the large number of volatile organic compounds present in human breath [194, 195]. The CE-DFCS technique has the potential to address this issue due to its capability of simultaneous multispecies detection.

The first test of the applicability of CE-DFCS for analysis of breath samples was conducted by Thorpe *et al.* [57]. The experimental setup with breath sampling is shown in Fig. 8.13(a) and was based on a 100-MHz Er:fiber OFC and a VIPA spectrometer (see Sect. 8.4.2). The comb light was coupled into an enhancement cavity with an *FSR* of 100 MHz and a finesse of 28000 using the swept coupling scheme (see Sect. 8.3.2). The laser generated a 100-nm-wide spectrum centered at 1.55 μm and could be shifted to the 1.6–1.7 μm region by Raman shifting in the amplifier, which also increased the average power to 300 mW.

The first experiment focused on the detection of CO and CO_2 near 1565 nm, as marked in Fig. 8.13(b). Breath samples were measured from two different

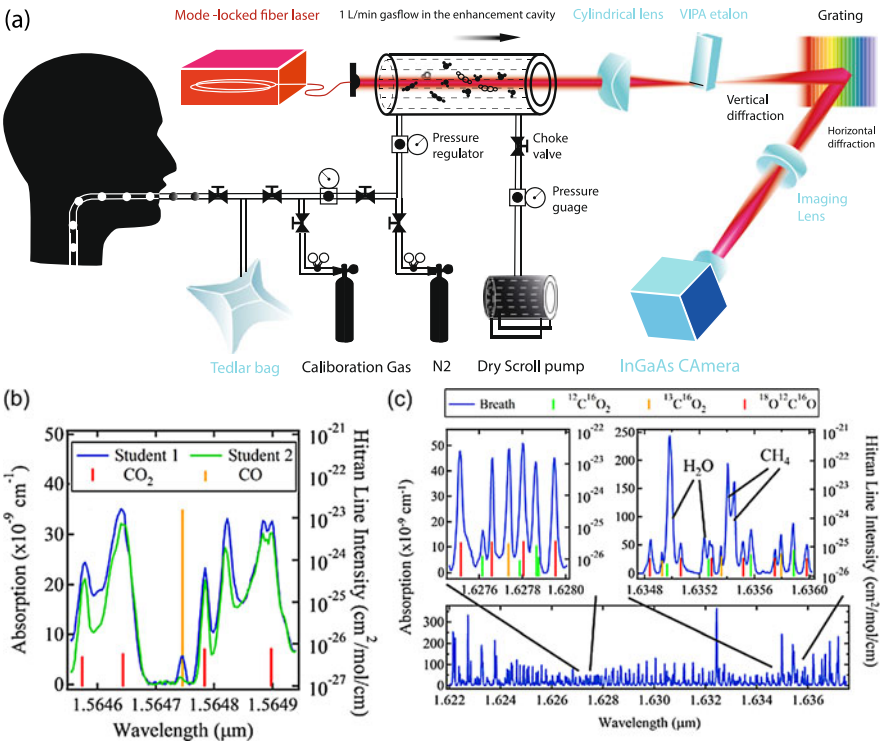

Fig. 8.13 Breath analysis with CE-DFCS around 1.6 μm. (**a**) The experimental setup including the breath sample handling system. (**b**) Zoomed-in view of two patients' breath spectra, showing measured absorption lines of CO_2 and CO (continuous spectrum) and the positions of CO_2 and CO lines from HITRAN (*red* and *yellow bars*, respectively). (**c**) A breath spectrum between 1.622 μm and 1.638 μm. Several windows in this region contain spectroscopic features of three isotopologues of CO_2, with nearly equal absorption strengths. Two zoomed-in spectral windows with line positions and intensities of relevant transitions are shown in the upper plots. Besides CO_2 peaks, strong absorption features of H_2O and CH_4 are detected in the measured spectral range (from Ref. [57])

students—one smoker (blue curve) and one non-smoker (green curve). The smoking student had a cigarette 15 minutes before the start of the test. The average concentration of CO for the smoker was determined to be 6.5 ppm—five times the value for the non-smoker. These results agree with previous studies of the CO level in a smoker's breath, ranging from 1 to 68 ppm [196]. In addition, a large change of the CO_2 concentration was observed as a function of time for which the patient held his breath before the sample was acquired, whereas the CO concentration was not influenced by the hold time.

The second test focused on the $^{13}C/^{12}C$ isotope ratio by comparing the concentrations of $^{13}CO_2$ and $^{12}CO_2$. This isotope ratio is of medical interest since it can provide information about liver function, bacterial overgrowth, or pancreatic function [197]; the main interest here was on the isotope ratio as a test for *helicobacter pylori* infection, which is a common cause of ulcers [198]. The infection

usually does not cause any visible symptoms, and it is estimated that two-thirds of the world population is infected with *helicobacter pylori* [199], so there is a need for a quick, non-invasive detection method allowing for screening of this infection in a large population.

The lower panel of Fig. 8.13(c) shows the absorption spectrum of breath from a healthy patient centered around 1.63 μm. In the wavelength range shown, there are 78 lines from $^{12}CO_2$ and 29 from $^{13}CO_2$. The two zoomed-in panels show that even in the presence of water and methane, the absorption lines of $^{12}CO_2$ and $^{13}CO_2$ are clearly visible. Using five lines for each isotope, an isotope ratio of $\delta^{13}C$ of -28.1 ± 4.1 was determined ($\delta^{13}C$ is defined as the difference in the isotope abundance from natural abundance in parts per thousand). Similar precision was obtained for $\delta^{18}O$, derived from the intensities of ^{18}OCO lines also present in this wavelength range. The precision of these measurements can be improved by including a larger number of lines in the multiline fit, with no cost in the measurement time. Since a precision of 1 part per thousand is more than suitable for a *helicobacter pylori* test [197], this experiment demonstrates the ability to simultaneously record multiple stable isotope ratios at clinically relevant levels.

With small changes to the experimental setup, for example by using a multi-branch laser, it would be possible to combine these two tests into a single measurement. The potential to identify a large number of compounds in a single sample of gaseous mixture is important for medical applications where samples can be challenging or time consuming to obtain. Mid-IR frequency combs provide access to many more molecular species of interest and may allow construction of a bench-top device capable of detecting bio-markers of multiple diseases in a single, quick test.

8.5.2 Trace Water in Arsine Vapor

Another application of CE-DFCS is monitoring of trace impurities in process gasses, such as silane (SiH_4), germane (GeH_4), phosphine (PH_3), and arsine (AsH_3), used in the semiconductor industry. Trace levels of contaminants (down to the tens-of-ppb level) in these process gasses have a direct negative impact on the performance and lifetime of the final products owing to the incorporation of donor or acceptor impurity sites in the semiconductor. Some of the main impurities of concern include oxygen, carbon dioxide, hydrocarbons such as methane and ethane, hydrogen sulfide, and water vapor [200–202]. Currently, different systems are used to monitor each contaminant, many of which are bulky or very slow. In particular, on-line monitoring of water contamination of the process gasses is important, since this contaminant is difficult to remove completely due to its low vapor pressure.

Laser-based gas monitoring has obvious advantages—it allows real-time analysis and unambiguous identification of molecules. The main problem with the detection of these impurities using absorption spectroscopy is the dense spectrum of the process gasses themselves, especially since these gases are at nearly 100 % purity, so the contaminant absorption is extremely weak compared to the absorption background

of the process gas. In addition, the possibility for rapid, simultaneous monitoring of multiple contaminants would be desirable. All these issues can be addressed with broadband CE-DFCS to achieve the required detection limits.

A CE-DFCS system focusing on detecting ppb levels of water contamination in arsine gas was constructed [56]. Due to the density of the arsine spectrum, the system was designed to work in the 1.75–1.95 μm wavelength region, where the arsine spectrum was previously unexplored but was expected to have a transparency window. To obtain an optical frequency comb in this wavelength range, the spectrum of an Er:fiber mode-locked laser, which provided 150 mW of power at a 250-MHz repetition rate, was amplified to 400 mW in an Er:fiber amplifier and was subsequently spectrally broadened in a 6-cm-long piece of highly-nonlinear silica fiber. The spectrum covered 1.2–2.1 μm and provided 17 mW of average power in a 40-nm bandwidth around 1.86 μm. The light was coupled into a 60-cm long enhancement cavity with a finesse of 30000 using the swept coupling scheme (see Sect. 8.3.2) [43]. In this case, f_{rep} was modulated at 7.5 kHz with a sweep amplitude for one comb tooth of 150 kHz in the optical domain. Slow feedback to the cavity PZT maintained the high transmission of the cavity for extended periods of time. A VIPA spectrometer [described in Sect. 8.4.2 and shown schematically in Fig. 8.7(c)] was used for detection, providing a spectral resolution of 900 MHz (0.031 cm^{-1}) and a simultaneous spectral coverage of 20 nm (50 cm^{-1}), limited by the size of the camera. Over 2000 spectral channels were collected simultaneously within 150 ms of integration time for a single image; typically 20 images were averaged per single spectrum.

Figure 8.14 shows the spectrum of 160 Torr of arsine gas contaminated with 1.27 ppm of water. The measured absorption spectrum is shown negative in black, with the water line strengths and positions from HITRAN [211] shown positive in blue. Even though the absorption of arsine gas increases rapidly close to the edges of the measured spectrum, a good transparency window does exist and allows for clear identification of water lines, visible in the two zoomed-in panels. The absorption sensitivity for water in arsine was determined to be 2.4×10^{-8} cm^{-1}, with a total integration time of 600 s. The sensitivity is limited by the background arsine absorption and by the low gas-switching speed as the initial gas handling system was not built for this application. This sensitivity corresponds to a minimum detectable absorption of 31 ppb for the trace amount of water in pure arsine. In summary, the system determined the required transmission window of arsine absorption and reached a detection limit suitable for the semiconductor industry.

8.5.3 Trace Detection of Hydrogen Peroxide

Another case where the absorption spectrum of a target molecule overlaps with spectra of more strongly absorbing or more abundant species is the detection of hydrogen peroxide (H_2O_2)—a molecule of interest for medical human breath analysis as well as atmospheric chemistry. In medicine, H_2O_2 is a potential marker of oxidative stress in the lungs, which can be connected to diseases such as asthma,

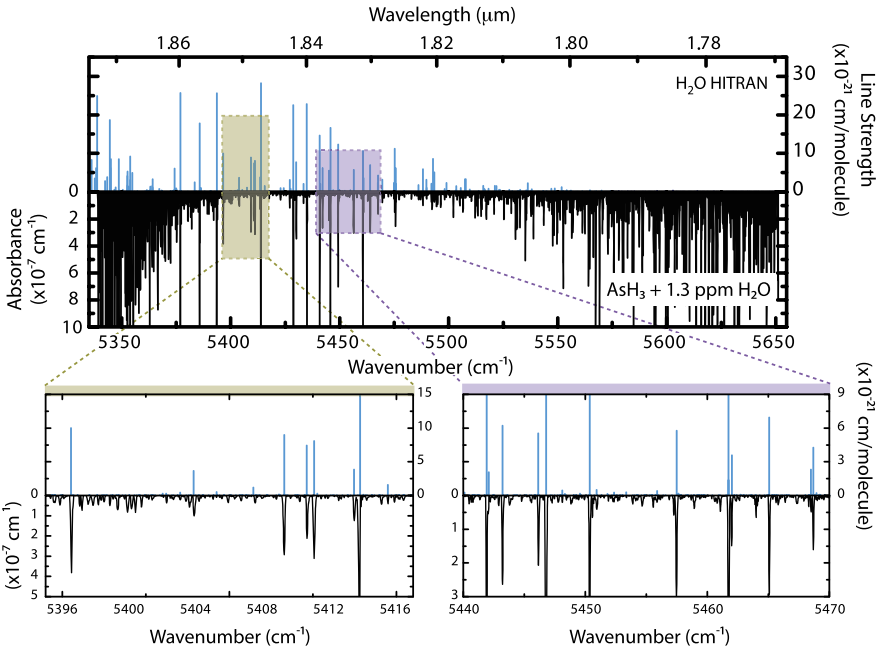

Fig. 8.14 Detection of water impurities in arsine process gas. The measured absorption spectrum of 1.27 ppm of water vapor in arsine is plotted negative (*black*) and the strengths of water lines taken from HITRAN are plotted positive (*blue*). The arsine absorption continues to increase both above 5650 cm^{-1} and below 5350 cm^{-1}. The *two bottom panels* with expanded views show easily resolvable water lines even in a strongly absorbing background gas (from Ref. [56]. With kind permission from Springer Science+Business Media: Appl. Phys. B, Analysis of trace impurities in semiconductor gas via cavity-enhanced direct frequency comb spectroscopy, vol. 100, year 2010, p. 917, K.C. Cossel et al., Fig. 4)

chronic obstructive pulmonary disease (COPD), or acute respiratory distress syndrome (ARDS) [203–205]. In atmospheric chemistry, H_2O_2 has a significant role as a stratospheric reservoir for HO_x [206] and is associated with biomass burning [207, 208]. However, the detection of this molecule is difficult since it is highly reactive and its fundamental ν_1 and ν_5 vibration bands overlap with strong absorption bands of water [209], which is usually the main interfering species, particularly in breath analysis (where water is present at a concentration of a few percent). The traditional approach used in breath analysis relies on water removal from the sample by filtering or on the use of exhaled breath condensate, both of which exclude real time operation. To test the possibility of real time monitoring of H_2O_2 concentration in gas samples with high water background, the H_2O_2 $\nu_2 + \nu_6$ intercombination band was targeted with a mid-infrared CE-DFCS system. This band, at 3.76 μm, is far detuned from all strong water absorption features and yet it is strong enough to provide sufficient detection limits [209, 210].

The experimental setup, shown in Fig. 8.6, was based on the tunable OPO comb and Fourier-transform spectrometer with auto-balanced detection described in

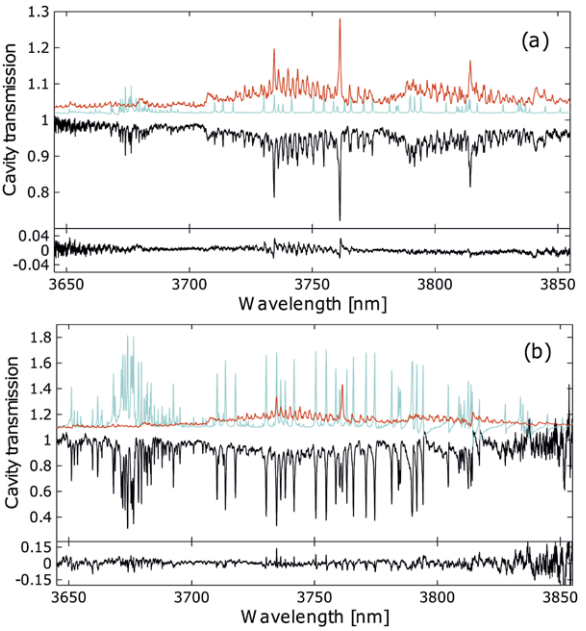

Fig. 8.15 Spectra of H_2O_2 solution vapor measured with mid-infrared CE-DFCS. In both panels the experimental spectra are shown in *black*, while the fit spectra of water and hydrogen peroxide in *blue* and *red*, respectively, inverted and offset for clarity. The *lower plots in each panel* display the fit residuals. (**a**) Spectrum taken at a pressure 630 Torr and room temperature with a small amount of N_2 flowing through the cavity spacer tube. The concentration values returned by the fit were 645 ppm for water and 3.6 ppm for H_2O_2. (**b**) Spectrum taken in 630 Torr of air and at a temperature of 37 °C with no N_2 flow through the cavity spacer tube. The concentration values returned by the fit were 1.2 % for water and 5 ppm for H_2O_2 (from Ref. [156]. With kind permission from Springer Science+Business Media: Appl. Phys. B, Cavity-enhanced optical frequency comb spectroscopy in the mid-infrared application to trace detection of hydrogen peroxide, vol. 110, year 2013, p. 163, A. Foltynowicz et al., Fig. 6)

Sects. 8.2.2 and 8.4.3, respectively. The enhancement cavity was constructed with two mirrors on ZnSe substrates and had a peak finesse of 3800 at 3.8 μm. The cavity length was chosen to be 54.7 cm so that the *FSR* was twice the comb repetition rate. The cavity was equipped with a glass container in which a liquid sample could be introduced, as well as a gas inlet and outlet allowing for constant flow of gaseous samples. This container was filled with a solution of 27 % of H_2O_2 in water to create a gaseous sample of hydrogen peroxide in the cavity. The surface of the peroxide solution was 6 cm below the cavity axis. The frequency comb was locked to the cavity with a two-point PDH lock (Sect. 8.3.1).

Figure 8.15(a) shows the normalized spectrum (in black) of the hydrogen peroxide vapor at a pressure of 630 Torr and at room temperature. To reduce the amount of water in the sample, a small flow of N_2 was maintained though the cavity during the measurement. The sum of model spectra of H_2O (from HITRAN [211]) and H_2O_2 (from [209]) was fit to the data; the constituent spectra from the fit are shown in

color (blue for H_2O and red for H_2O_2, inverted and offset for clarity). A sensitivity of 5.4×10^{-9} cm^{-1} Hz$^{-1/2}$ was reached, corresponding to 6.9×10^{-11} cm^{-1} Hz$^{-1/2}$ per spectral element for 6000 resolved elements. This resulted in a noise equivalent concentration detection limit for H_2O_2 in the absence of water of 8 ppb for 1 s averaging time.

To simulate the conditions of human breath analysis, the container and the cavity cell were heated to a temperature of 37 °C and the N_2 purge was turned off. To avoid water condensation on the cavity mirror surfaces, the mirrors were heated to around 40 °C. Under these conditions, water absorption dominated the measured spectrum, as can be seen in Fig. 8.15(b); however, it was still possible to observe absorption due to hydrogen peroxide. The concentrations obtained from the fit are 5 ppm of H_2O_2 and 1.2 % of H_2O. It can be seen that the discrepancies in the center of the fit are larger than those for the low concentration case, suggesting that water was affecting the detection limit of H_2O_2.

To estimate the effects of water on the detection limit of hydrogen peroxide, pure deionized water was introduced into the container and the spectra of its vapor in air were recorded. The temperature and pressure conditions were the same as those for the hydrogen peroxide measurement at elevated temperature shown in Fig. 8.15(b). A model including both H_2O and H_2O_2 was fit to 100 consecutively measured spectra and a mean H_2O and H_2O_2 concentrations of 2.83 % and 75 ppb were obtained, respectively, with a standard deviation of 130 ppb in the second case, which implies a detection limit of 130 ppb for H_2O_2 in the presence of almost 3 % of water. This value is significantly higher than that expected from the noise level; however, for the detection of a weak absorption signal out of overlapping strong absorption background of other constituents, the detection limit for the weak component is set by the quality of the model spectra of the strong components rather than by the detection noise. To remove this limitation, the spectra of the strong components need to be precisely determined under the relevant experimental conditions, including effects not described by the Voigt profile such as Dicke narrowing or the speed dependence of both pressure broadening and shifting [212, 213], which are not included in the HITRAN database. Thus, systematic analysis of the line shapes for the overlapping water band will be critical for further performance improvements.

This experiment was the first demonstration of CE-DFCS in the mid-IR region and confirmed that it is capable of efficient detection of H_2O_2 at the sub-ppm level even in the presence of a large amount of water, without the need for water removal. The data obtained with low water concentration [Fig. 8.15(a)] suggest that the CE-DFCS technique allows detection of H_2O_2 using the $\nu_2 + \nu_6$ band down to the low ppb level. While this detection limit is not as low as that of a cw-laser based system used for atmospheric research [214], CE-DFCS offers the capability for simultaneous detection of additional molecular species of interest such as methane, acetylene, nitrous oxide, and formaldehyde, in a single system.

It is interesting to compare the performance of this mid-IR CE-DFCS system to that based on the same OPO and FTS and employing a multipass cell instead of the cavity [48]. The absorption sensitivity obtained with the Herriot cell is significantly lower (3.8×10^{-8} cm^{-1} Hz$^{-1/2}$ per spectral element), mostly due to the

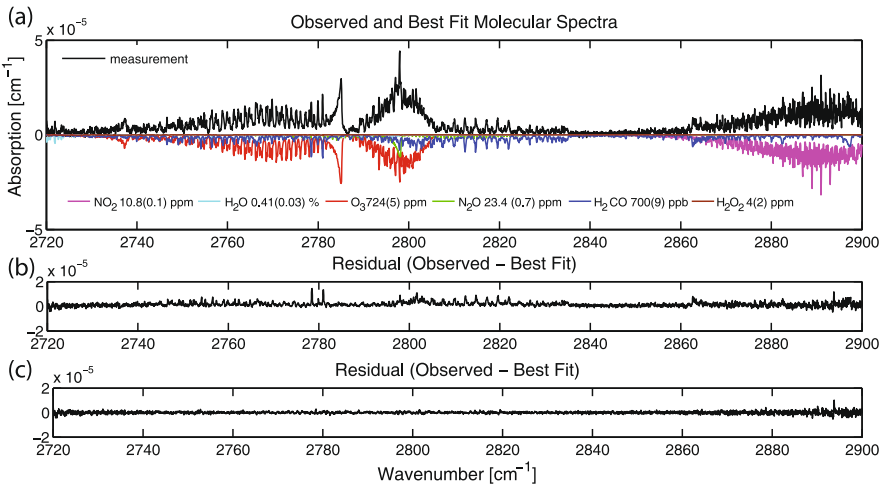

Fig. 8.16 (**a**) The absorption spectrum of the plasma effluent (*black*) at a pressure of 620 Torr measured around 3.6 μm (2800 cm^{-1}), recorded at 28 s after the plasma is turned on. The individual molecular spectra (*magenta*—nitrogen dioxide, *red*—ozone, *grey*—water, *green*—nitric oxide, *blue*—formaldehyde, *brown*—hydrogen peroxide), whose sum is fit to the measured data, are plotted negative for clarity. The legend lists the fit concentrations with 1σ uncertainties. (**b**) The residual of the fit for the case when the spectrum of formaldehyde is not included in the model. (**c**) The residual of the fit when a model including all the mixture components is applied (from Ref. [26])

difference in effective path length (36 m inside the cell, compared to 1.3 km in the cavity), and the lack of autobalanced detection in the experiment with the multipass cell. However, the multipass cell allows acquisition of spectra over the entire tuning range (2.8–4.6 μm) of the OPO, as was demonstrated in Ref. [48], while the cavity effectively limits the useful bandwidth, as shown in Fig. 8.5.

The mid-IR system with multipass cell was used in an experiment that nicely demonstrates the general capabilities of DFCS. It was employed for measurements of hydrogen-peroxide-enhanced non-thermal plasma effluent, created in a device made for disinfection purposes in various medical settings [26]. The multipass cell was connected to the plasma device, taking the place of a disinfection chamber and the device ran in a closed-loop configuration maintaining a constant flow of disinfection gas mixture through the cell. The mixture was expected to be a combination of constituents such as O_3, N_2O, NO_2, NO, OH* and H_2O_2: the latter was added separately to enhance the disinfection performance as confirmed by separate tests with bacteria [26]. To optimize the disinfection efficiency, quantitative information on the concentration levels of individual constituents under different plasma operating conditions was needed.

Figure 8.16 shows an example of the experimental spectrum of plasma effluent at a pressure of 620 Torr. Panel (a) shows the measured absorption spectrum (black) and the model spectra of the individual constituents (plotted negative for clarity, in color), whose sum is fit to the experimental data. Panel (b) plots the fit residuals from

the model including all expected species visible in the spectral window (O_3, N_2O, NO_2 and H_2O_2). The structure in the residual indicates that the assumed model of the spectrum did not account for all the absorbing species produced by the medical device. Indeed, the fit significantly improves after adding H_2CO (initially not expected in the mixture) spectrum to the model, as shown by the residuals in panel (c). The obtained values of the single components concentrations with 1σ uncertainties are shown in panel (a).

The broadband coverage of DFCS enables precise determination of concentrations of multiple molecular species simultaneously without *a priori* knowledge of all constituents. Such capability is desirable for many scientific applications, including atmospheric research and breath analysis, and is difficult to realize with cw-laser based systems; even if multiple cw lasers would be used, their frequencies would be set to transitions of constituents expected to be present in the mixture, precluding the observation of unexpected features. The fact that the full spectrum is acquired simultaneously eliminates drifts across the spectrum due to the scanning time of cw lasers. Although the presented example does not employ a cavity, a similar application with a cavity-based system is straightforward.

8.5.4 Comb-Mode Resolved Spectroscopy

The examples described above focus on spectroscopic applications of CE-DFCS without the need to resolve individual comb lines. Below we present two different applications demonstrating the advantages of simultaneously acquiring spectra with comb-mode resolution. In the first example, the enhanced resolution permits detailed examinations of both translational and rotational cooling in a supersonic molecular beam expansion. In the second example, modulation and lock-in detection are introduced to CE-DFCS, allowing high-resolution velocity-modulation spectroscopy of molecular ions to be performed on many comb lines simultaneously.

Spectroscopy of Cold Molecules Pulsed supersonic expansions are widely used in physical chemistry and molecular physics to obtain internal cooling of molecules without the need for cryogenic systems. The cooling dynamics in such systems can be complex and depend not only on the species to be cooled and the nozzle geometry, but also on the carrier gas species, backing pressure, and background pressure. Thus, the cooling in a supersonic expansion is often both spatially dependent and internal state dependent (i.e., the rotational, vibrational, and electronic temperatures are not in equilibrium).

Rapid tomography of a pulsed supersonic expansion of 2 % acetylene seeded in argon has been demonstrated using CE-DFCS [60]. A cavity with an *FSR* of 700 MHz and a finesse of 6300, centered at the 1.53 μm ($\nu_1 + \nu_3$) acetylene band, was aligned perpendicular to the molecular jet direction. Thus, the cavity mode measured a small, cylindrical region of the molecular beam expansion, perpendicular to the beam propagation direction. The expansion nozzle position was translatable *in situ* in three dimensions, which results in the cavity mode sampling different regions

of the expansion. The light from an Er:fiber frequency comb ($f_{rep} = 100$ MHz) was coupled into the cavity using the swept coupling scheme. The cavity increased the comb mode spacing to the cavity *FSR*, so that only one comb mode interacted with a given molecular ro-vibrational line (with approximately 300 MHz linewidth) at a time. This provides single comb-mode resolution since only one ro-vibrational line occurred within the VIPA spectrometer resolution. The cavity length was actively stabilized to an iodine-stabilized reference laser and was scanned over one *FSR* by shifting the reference laser frequency.

The comb light transmitted through the cavity was recorded using a VIPA spectrometer (see Sect. 8.4.2). The camera integration time was synchronized with the gas pulse to enable gating of specific regions of the pulse. To create a full tomographic reconstruction of the expansion, a spectrum at a given nozzle position was measured by stepping the cavity length over one *FSR*; this process was then repeated for different transverse and longitudinal positions of the nozzle. Each spectrum contains a wealth of information: first, by integrating over the width of each ro-vibrational line, a rotational distribution integrated along the cavity axis was obtained. By using measurements at different heights, and relying on the cylindrical symmetry of the expansion, a radial density and temperature profile of the expansion could be derived. In addition, individual ro-vibrational line shapes, as shown in Fig. 8.17(a), could be analyzed in detail. These Doppler-broadened line shapes provided information about transverse-velocity and rotational-state dependent effects. For example, in the shaded regions, an increased population in lower rotational states relative to higher rotational states was observed, which suggests that the cooling was optimal off the molecular beam axis (i.e., in regions with non-zero transverse velocity), potentially due to on-axis clustering.

This experiment illustrates how CE-DFCS combines the seemingly incompatible capabilities of wide spectral bandwidth, high sensitivity, sub-millisecond temporal resolution, and high spectral resolution, all in one experimental platform. In this case, the wide, simultaneous spectral bandwidth along with the temporal resolution provided information about the rotational cooling as a function of the spatial and the temporal positions in the gas pulse. The single comb mode resolution enabled simultaneous comparison of the line shapes of many ro-vibrational lines. This makes CE-DFCS a potentially powerful tool for studying state-dependent collisions and reactions in applications such as crossed molecular beams, trapped cold and ultracold molecules, and studies of unstable intermediates in chemical reactions.

Velocity Modulation Spectroscopy Broadband spectroscopy of molecular ions has many applications in areas ranging from fundamental physics to physical chemistry and astrochemistry. In astrochemistry, for example, it is believed that many of the currently unidentified visible to near-IR absorption bands, collectively termed the diffuse interstellar bands (DIBs), may be due to interstellar absorption from molecular ions [215, 216]. Molecular ions also hold potential for precision measurements [217–221] such as testing QED calculations, tests of time variation of the electron-to-proton mass ratio and the fine structure constant, or measurement of the permanent electric dipole moment of the electron (eEDM) due to the long coherence times possible with trapped ions.

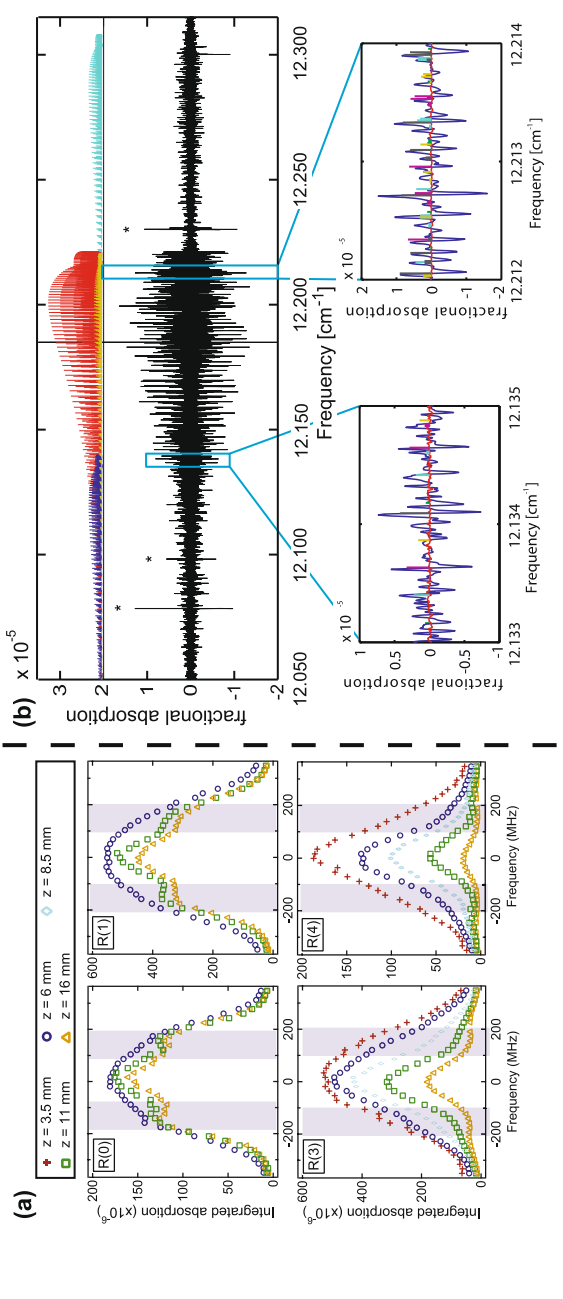

Fig. 8.17 Comb-mode resolved CE-DFCS. (**a**) Line shapes of four ro-vibrational lines in the R-branch of the acetylene $\nu_1 + \nu_3$ band recorded in a pulsed supersonic expansion as a function of distance from the nozzle. Notice that lower J lines (*upper two plots*) show an increase in population in the shaded regions compared with the higher J lines (*two lower plots*) [60]. (**b**) The spectrum of HfF^+ recorded with CE-DFCS combined with velocity modulation spectroscopy. Fits to four different ro-vibronic bands are shown above the experimentally obtained spectrum. The *insets* show the high-resolution spectra, with individual isotopes (marked in different colors) clearly resolved

One of the challenges in using molecular ions for precision measurement is a lack of available spectroscopic data. For example, in the JILA eEDM experiment multiple states of HfF^+ or ThF^+ [222] will be needed for state preparation and spin readout; thus a method for broad survey spectroscopy to characterize the electronic structure of these ions was needed. Pulsed-field-ionization zero-kinetic-energy measurements (PFI-ZEKE) recently provided information about the lowest lying states of HfF^+ [223] and ThF^+ [224]. Theoretical calculations exist for the states of HfF^+, but due to the challenges of including so many electrons in the calculations, the uncertainties were at least a thousand wavenumbers [225].

Recently, CE-DFCS has been incorporated into velocity-modulation spectroscopy (VMS) to enable broadband, ion-specific detection [58, 59]. In this experiment, a 3-GHz repetition rate Ti:sapphire comb was locked (using a single-point tight lock) to a ring cavity with an *FSR* equal to $1/25$ of f_{rep} and a finesse of about 100. The cavity contained an AC discharge cell that both produced the ions and modulated their drift velocity, resulting in a modulated absorption signal. The transmitted comb light was comb-mode resolved by the VIPA spectrometer and imaged onto a lock-in camera, which simultaneously demodulated each pixel (and thus each comb tooth) at the discharge frequency. Polarization optics were used to rapidly switch the direction of light propagation through the cavity for noise reduction.

About 1500 channels, spanning 150 cm^{-1}, were recorded simultaneously. One comb tooth was locked to a stable cw Ti:sapphire laser, which provided an absolute frequency reference in our spectrum. For each measurement, images for each direction of propagation were averaged and subtracted. Additionally, the power in each comb tooth was measured by applying a calibrated amplitude modulation to the laser. To fully sample the spectrum, 30 measurements with the cw laser stepped over 3 GHz were interleaved. This resulted in a spectrum that covered 150 cm^{-1} sampled with a step-size of 100 MHz. The spectrum was then interpolated onto a fixed 0.001 cm^{-1} grid to allow scans to be easily averaged or combined. One full scan lasted about 30 minutes and resulted in a single-pass fractional absorption sensitivity of 3×10^{-7}. Since one scan contained 45000 channels, this equated to a sensitivity of 4×10^{-8} $\mathrm{Hz}^{-1/2}$ per spectral element.

The top panel of Fig. 8.17(b) shows part of the HfF^+ spectrum acquired using the comb-VMS system, with the different observed ro-vibronic bands shown above in different colors. The spectrum centered around 12200 cm^{-1} is extremely congested due to the presence of many bands, each with five isotopes, and the high temperature of the oven, which results in observed J values up to about 70. The dynamic range of frequency-comb VMS is demonstrated by our ability to identify two overlapping vibronic bands (shown in red and green) despite an order of magnitude difference in line strengths and an offset in the band origin of only about 1 cm^{-1}. Since wide spectral windows are acquired simultaneously when using the comb, relative line strengths within the region are not influenced by variability in oven and discharge conditions, which significantly helped to disentangle the bands. The total spectral coverage of the system is extendable using nonlinear optics or different comb sources as discussed earlier. This technique is thus a powerful system for accurate survey spectroscopy of many molecular ion species over a wide spectral range.

8.6 Summary

This chapter discusses the principles of the CE-DFCS technique and reviews existing frequency comb sources ranging from the XUV to the mid-IR. Methods of coupling and locking frequency combs to an enhancement cavity are presented, as are different read-out systems capable of simultaneous acquisition of thousands of channels. Combined, these techniques represent the current state of the art of CE-DFCS; however, the rapid progress in this field guarantees improvements in spectral coverage, absorption sensitivity, and acquisition rate. Development of new frequency comb sources and improved properties of their spectra will enable access to molecular and atomic systems in previously unaccessible spectral regions.

An overview of various systems and applications of the technique was presented to highlight the different combinations of broadband coverage, high resolution, and ultra-high sensitivity provided by CE-DFCS. In a number of research areas, such as breath analysis, trace detection of contaminants in industrial gases, or atmospheric chemistry, the enormous potential is just starting to be recognized. We are confident that new windows of opportunity will arise in other fields, including precision spectroscopy, studies of molecular interaction and reaction dynamics, and coherent control of atomic or molecular systems.

Acknowledgements We gratefully thank many of our colleagues who have contributed to the work described in this review. They are F. Adler, T. Allison, T. Ban, C. Benko, B. Bjork, T. Briles, A. Cingöz, E. Cornell, S. Diddams, M. Fermann, A. Fleisher, M. Golkowski, J. Hall, I. Hartl, L.-S. Ma, M. Martin, J. Repine, A. Ruehl, L. Sinclair, M. Thorpe, and D. Yost. The development of CE-DFCS has been supported by NIST, AFOSR, DARPA, NSF, DTRA, and Agilent.

References

1. S.A. Diddams et al., Direct link between microwave and optical frequencies with a 300 THz femtosecond laser comb. Phys. Rev. Lett. **84**(22), 5102–5105 (2000)
2. R. Holzwarth et al., Optical frequency synthesizer for precision spectroscopy. Phys. Rev. Lett. **85**(11), 2264–2267 (2000)
3. T. Udem, R. Holzwarth, T.W. Hansch, Optical frequency metrology. Nature **416**(6877), 233–237 (2002)
4. S.T. Cundiff, J. Ye, Colloquium: femtosecond optical frequency combs. Rev. Mod. Phys. **75**(1), 325–342 (2003)
5. J. Ye, S.T. Cundiff (eds.), *Femtosecond Optical Frequency Comb: Principle, Operation, and Applications* (Springer, Berlin, 2004)
6. T.W. Hansch, Nobel lecture: passion for precision. Rev. Mod. Phys. **78**(4), 1297–1309 (2006)
7. J.L. Hall, Nobel lecture: defining and measuring optical frequencies. Rev. Mod. Phys. **78**(4), 1279–1295 (2006)
8. S.A. Diddams, The evolving optical frequency comb. J. Opt. Soc. Am. B, Opt. Phys. **27**(11), B51–B62 (2010)
9. L.S. Ma et al., Optical frequency synthesis and comparison with uncertainty at the 10^{-19} level. Science **303**(5665), 1843–1845 (2004)
10. A. Bartels et al., Stabilization of femtosecond laser frequency combs with subhertz residual linewidths. Opt. Lett. **29**(10), 1081–1083 (2004)

11. T.R. Schibli et al., Optical frequency comb with submillihertz linewidth and more than 10 W average power. Nat. Photonics **2**(6), 355–359 (2008)
12. M.J. Martin et al., Testing ultrafast mode-locking at microhertz relative optical linewidth. Opt. Express **17**(2), 558–568 (2009)
13. S.M. Foreman et al., Coherent optical phase transfer over a 32-km fiber with 1 s instability at 10^{-17}. Phys. Rev. Lett. **99**(15), 153601 (2007)
14. S.M. Foreman et al., Remote transfer of ultrastable frequency references via fiber networks. Rev. Sci. Instrum. **78**(2), 021101 (2007)
15. A.D. Ludlow et al., Sr lattice clock at 1×10^{-16} fractional uncertainty by remote optical evaluation with a Ca clock. Science **319**(5871), 1805–1808 (2008)
16. K. Predehl et al., A 920-kilometer optical fiber link for frequency metrology at the 19th decimal place. Science **336**(6080), 441–444 (2012)
17. O. Lopez et al., Ultra-stable long distance optical frequency distribution using the Internet fiber network. Opt. Express **20**(21), 23518–23526 (2012)
18. A. Ruehl et al., Ultrabroadband coherent supercontinuum frequency comb. Phys. Rev. A **84**(1), 011806(R) (2011)
19. N.R. Newbury, Searching for applications with a fine-tooth comb. Nat. Photonics **5**(4), 186–188 (2011)
20. T. Steinmetz et al., Laser frequency combs for astronomical observations. Science **321**(5894), 1335–1337 (2008)
21. D.A. Braje et al., Astronomical spectrograph calibration with broad-spectrum frequency combs. Eur. Phys. J. D **48**(1), 57–66 (2008)
22. G.G. Ycas et al., Demonstration of on-sky calibration of astronomical spectra using a 25 GHz near-IR laser frequency comb. Opt. Express **20**(6), 6631–6643 (2012)
23. T. Wilken et al., A spectrograph for exoplanet observations calibrated at the centimetre-per-second level. Nature **485**(7400), 611–614 (2012)
24. D.F. Phillips et al., Calibration of an astrophysical spectrograph below 1 m/s using a laser frequency comb. Opt. Express **20**(13), 13711–13726 (2012)
25. S.J. Lee et al., Ultrahigh scanning speed optical coherence tomography using optical frequency comb generators. Jpn. J. Appl. Phys. **40**(8B), L878–L880 (2001)
26. M. Golkowski et al., Hydrogen-peroxide-enhanced nonthermal plasma effluent for biomedical applications. IEEE Trans. Plasma Sci. **40**(8), 1984–1991 (2012)
27. A. Bartels et al., Femtosecond-laser-based synthesis of ultrastable microwave signals from optical frequency references. Opt. Lett. **30**(6), 667–669 (2005)
28. T.M. Fortier et al., Generation of ultrastable microwaves via optical frequency division. Nat. Photonics **5**(7), 425–429 (2011)
29. T. Udem et al., Absolute optical frequency measurement of the cesium D1 line with a mode-locked laser. Phys. Rev. Lett. **82**(18), 3568–3571 (1999)
30. A. Marian et al., United time-frequency spectroscopy for dynamics and global structure. Science **306**(5704), 2063–2068 (2004)
31. M.C. Stowe et al., High resolution atomic coherent control via spectral phase manipulation of an optical frequency comb. Phys. Rev. Lett. **96**(15), 153001 (2006)
32. J. Ye et al., Accuracy comparison of absolute optical frequency measurement between harmonic-generation synthesis and a frequency-division femtosecond comb. Phys. Rev. Lett. **85**(18), 3797–3800 (2000)
33. T.W. Hansch et al., Precision spectroscopy of hydrogen and femtosecond laser frequency combs. Philos. Trans. R. Soc., Math. Phys. Eng. Sci. **363**(1834), 2155–2163 (2005)
34. G. Galzerano et al., Absolute frequency measurement of a water-stabilized diode laser at 1.384 μm by means of a fiber frequency comb. Appl. Phys. B, Lasers Opt. **102**(4), 725–729 (2011)
35. I. Galli et al., Molecular gas sensing below parts per trillion: radiocarbon-dioxide optical detection. Phys. Rev. Lett. **107**(27), 270802 (2011)
36. J. Domyslawska et al., Cavity ring-down spectroscopy of the oxygen B-band with absolute frequency reference to the optical frequency comb. J. Chem. Phys. **136**(2), 024201 (2012)

37. I. Ricciardi et al., Frequency-comb-referenced singly-resonant OPO for sub-Doppler spectroscopy. Opt. Express **20**(8), 9178–9186 (2012)
38. M. Fischer et al., New limits on the drift of fundamental constants from laboratory measurements. Phys. Rev. Lett. **92**(23), 230802 (2004)
39. G. Casa et al., Primary gas thermometry by means of laser-absorption spectroscopy: determination of the Boltzmann constant. Phys. Rev. Lett. **100**(20), 200801 (2008)
40. C.G. Parthey et al., Improved measurement of the hydrogen 1S–2S transition frequency. Phys. Rev. Lett. **107**(20), 203001 (2011)
41. C. Lemarchand et al., Progress towards an accurate determination of the Boltzmann constant by Doppler spectroscopy. New J. Phys. **13**, 073028 (2011)
42. A. Marian et al., Direct frequency comb measurements of absolute optical frequencies and population transfer dynamics. Phys. Rev. Lett. **95**(2), 023001 (2005)
43. M.J. Thorpe, J. Ye, Cavity-enhanced direct frequency comb spectroscopy. Appl. Phys. B, Lasers Opt. **91**(3–4), 397–414 (2008)
44. F. Adler et al., Cavity-enhanced direct frequency comb spectroscopy: technology and applications. Annu. Rev. Anal. Chem. **3**(3), 175–205 (2010)
45. A. Foltynowicz et al., Optical frequency comb spectroscopy. Faraday Discuss. **150**, 23–31 (2011)
46. J.U. White, Long optical paths of large aperture. J. Opt. Soc. Am. **32**(5), 285–288 (1942)
47. D.R. Herriott, H.J. Schulte, Folded optical delay lines. Appl. Opt. **4**(8), 883 (1965)
48. F. Adler et al., Mid-infrared Fourier transform spectroscopy with a broadband frequency comb. Opt. Express **18**(21), 21861–21872 (2010)
49. A.M. Zolot et al., Direct-comb molecular spectroscopy with accurate, resolved comb teeth over 43 THz. Opt. Lett. **37**(4), 638–640 (2012)
50. E.R. Crosson et al., Pulse-stacked cavity ring-down spectroscopy. Rev. Sci. Instrum. **70**(1), 4–10 (1999)
51. T. Gherman, D. Romanini, Mode-locked cavity-enhanced absorption spectroscopy. Opt. Express **10**(19), 1033–1042 (2002)
52. R.J. Jones, J. Ye, Femtosecond pulse amplification by coherent addition in a passive optical cavity. Opt. Lett. **27**(20), 1848–1850 (2002)
53. M.J. Thorpe et al., Broadband cavity ringdown spectroscopy for sensitive and rapid molecular detection. Science **311**(5767), 1595–1599 (2006)
54. G. Mejean, S. Kassi, D. Romanini, Measurement of reactive atmospheric species by ultraviolet cavity-enhanced spectroscopy with a mode-locked femtosecond laser. Opt. Lett. **33**(11), 1231–1233 (2008)
55. R. Grilli et al., Trace measurement of BrO at the ppt level by a transportable mode-locked frequency-doubled cavity-enhanced spectrometer. Appl. Phys. B, Lasers Opt. **107**(1), 205–212 (2012)
56. K.C. Cossel et al., Analysis of trace impurities in semiconductor gas via cavity-enhanced direct frequency comb spectroscopy. Appl. Phys. B, Lasers Opt. **100**(4), 917–924 (2010)
57. M.J. Thorpe et al., Cavity-enhanced optical frequency comb spectroscopy: application to human breath analysis. Opt. Express **16**(4), 2387–2397 (2008)
58. L.C. Sinclair et al., Frequency comb velocity-modulation spectroscopy. Phys. Rev. Lett. **107**(9), 093002 (2011)
59. K.C. Cossel et al., Broadband velocity modulation spectroscopy of HfF^+: towards a measurement of the electron electric dipole moment. Chem. Phys. Lett. **546**, 1–11 (2012)
60. M.J. Thorpe et al., Tomography of a supersonically cooled molecular jet using cavity-enhanced direct frequency comb spectroscopy. Chem. Phys. Lett. **468**(1–3), 1–8 (2009)
61. R.J. Jones et al., Phase-coherent frequency combs in the vacuum ultraviolet via high-harmonic generation inside a femtosecond enhancement cavity. Phys. Rev. Lett. **94**(19), 193201 (2005)
62. C. Gohle et al., A frequency comb in the extreme ultraviolet. Nature **436**(7048), 234–237 (2005)

63. A. Ozawa et al., High harmonic frequency combs for high resolution spectroscopy. Phys. Rev. Lett. **100**(25), 253901 (2008)
64. A. Cingoz et al., Direct frequency comb spectroscopy in the extreme ultraviolet. Nature **482**(7383), 68–71 (2012)
65. F. Keilmann, C. Gohle, R. Holzwarth, Time-domain mid-infrared frequency-comb spectrometer. Opt. Lett. **29**(13), 1542–1544 (2004)
66. K.A. Tillman et al., Mid-infrared absorption spectroscopy of methane using a broadband femtosecond optical parametric oscillator based on aperiodically poled lithium niobate. J. Opt. A, Pure Appl. Opt. **7**(6), S408–S414 (2005)
67. E. Sorokin et al., Sensitive multiplex spectroscopy in the molecular fingerprint 2.4 μm region with a Cr(2+): ZnSe femtosecond laser. Opt. Express **15**(25), 16540–16545 (2007)
68. F. Adler et al., Phase-stabilized, 1.5 W frequency comb at 2.8–4.8 μm. Opt. Lett. **34**(9), 1330–1332 (2009)
69. N. Leindecker et al., Broadband degenerate OPO for mid-infrared frequency comb generation. Opt. Express **19**(7), 6304–6310 (2011)
70. N. Leindecker et al., Octave-spanning ultrafast OPO with 2.6–6.1 μm instantaneous bandwidth pumped by femtosecond Tm-fiber laser. Opt. Express **20**(7), 7046–7053 (2012)
71. T. Udem et al., Accurate measurement of large optical frequency differences with a mode-locked laser. Opt. Lett. **24**(13), 881–883 (1999)
72. D.J. Jones et al., Carrier-envelope phase control of femtosecond mode-locked lasers and direct optical frequency synthesis. Science **288**(5466), 635–639 (2000)
73. A. Bartels, D. Heinecke, S.A. Diddams, 10-GHz self-referenced optical frequency comb. Science **326**(5953), 681 (2009)
74. T.M. Fortier, A. Bartels, S.A. Diddams, Octave-spanning Ti:sapphire laser with a repetition rate >1 GHz for optical frequency measurements and comparisons. Opt. Lett. **31**(7), 1011–1013 (2006)
75. J. Jiang et al., Fully stabilized, self-referenced thulium fiber frequency comb, in *The European Conference on Lasers and Electro-Optics* (Optical Society of America, Washington, 2011)
76. M.N. Cizmeciyan et al., Operation of femtosecond Kerr-lens mode-locked Cr:ZnSe lasers with different dispersion compensation methods. Appl. Phys. B, Lasers Opt. **106**(4), 887–892 (2012)
77. T.W. Neely, T.A. Johnson, S.A. Diddams, High-power broadband laser source tunable from 3.0 μm to 4.4 μm based on a femtosecond Yb:fiber oscillator. Opt. Lett. **36**(20), 4020–4022 (2011)
78. A. Ruehl et al., Widely-tunable mid-infrared frequency comb source based on difference frequency generation. Opt. Lett. **37**(12), 2232–2234 (2012)
79. M.E. Fermann, A. Galvanauskas, G. Sucha (eds.), *Ultrafast Lasers: Technology and Applications* (CRC Press, Boca Raton, 2002)
80. U. Keller, Recent developments in compact ultrafast lasers. Nature **424**(6950), 831–838 (2003)
81. J.-C. Diels, W. Rudolph, *Ultrashort Laser Pulse Phenomena*, 2nd edn. (Academic Press, New York, 2006)
82. U. Keller et al., Semiconductor saturable absorber mirrors (SESAM's) for femtosecond to nanosecond pulse generation in solid-state lasers. IEEE J. Sel. Top. Quantum Electron. **2**(3), 435–453 (1996)
83. C.C. Lee et al., Ultra-short optical pulse generation with single-layer graphene. J. Nonlinear Opt. Phys. Mater. **19**(4), 767–771 (2010)
84. H.J. Kim et al., High-performance laser mode-locker with glass-hosted SWNTs realized by room-temperature aerosol deposition. Opt. Express **19**(5), 4762–4767 (2011)
85. A. Schmidt et al., 175 fs Tm:Lu(2)O(3) laser at 2.07 μm mode-locked using single-walled carbon nanotubes. Opt. Express **20**(5), 5313–5318 (2012)
86. R.W. Boyd, *Nonlinear Optics*, 3rd edn. (Academic Press, New York, 2008)

87. D.E. Spence, P.N. Kean, W. Sibbett, 60-fsec pulse generation from a self-mode-locked Ti-sapphire laser. Opt. Lett. **16**(1), 42–44 (1991)
88. U. Keller et al., Femtosecond pulses from a continuously self-starting passively mode-locked Ti-sapphire laser. Opt. Lett. **16**(13), 1022–1024 (1991)
89. I.T. Sorokina, K.L. Vodopyanov (eds.), *Solid-State Mid-Infrared Laser Sources*. Topics in Applied Physics (Springer, Berlin, 2003)
90. M. Ebrahim-Zadeh, I.T. Sorokina (eds.), *Mid-Infrared Coherent Sources and Applications*. NATO Science for Peace and Security Series B: Physics and Biophysics. (Springer, Dordrecht, 2008)
91. M.N. Cizmeciyan et al., Kerr-lens mode-locked femtosecond Cr(2+):ZnSe laser at 2420 nm. Opt. Lett. **34**(20), 3056–3058 (2009)
92. F. Salin, J. Squier, M. Piche, Mode-locking of Ti-Al(2)O(3) lasers and self-focusing—a Gaussian approximation. Opt. Lett. **16**(21), 1674–1676 (1991)
93. H.A. Haus, E.P. Ippen, K. Tamura, Additive-pulse modelocking in fiber lasers. IEEE J. Quantum Electron. **30**(1), 200–208 (1994)
94. G. Agrawal, in *Nonlinear Fiber Optics*, 4th edn. (2006)
95. G. Genty, S. Coen, J.M. Dudley, Fiber supercontinuum sources (invited). J. Opt. Soc. Am. B, Opt. Phys. **24**(8), 1771–1785 (2007)
96. P. Russell, Photonic crystal fibers. Science **299**(5605), 358–362 (2003)
97. J.C. Knight, Photonic crystal fibres. Nature **424**(6950), 847–851 (2003)
98. L. Dong, B.K. Thomas, L.B. Fu, Highly nonlinear silica suspended core fibers. Opt. Express **16**(21), 16423–16430 (2008)
99. L.B. Fu, B.K. Thomas, L. Dong, Efficient supercontinuum generations in silica suspended core fibers. Opt. Express **16**(24), 19629–19642 (2008)
100. T. Okuno et al., Silica-based functional fibers with enhanced nonlinearity and their applications. IEEE J. Sel. Top. Quantum Electron. **5**(5), 1385–1391 (1999)
101. J.M. Dudley, S. Coen, Numerical simulations and coherence properties of supercontinuum generation in photonic crystal and tapered optical fibers. IEEE J. Sel. Top. Quantum Electron. **8**(3), 651–659 (2002)
102. P. Domachuk et al., Over 4000 nm bandwidth of mid-IR supercontinuum generation in sub-centimeter segments of highly nonlinear tellurite PCFs. Opt. Express **16**(10), 7161–7168 (2008)
103. J.S. Sanghera, L.B. Shaw, I.D. Aggarwal, Chalcogenide glass-fiber-based mid-IR sources and applications. IEEE J. Sel. Top. Quantum Electron. **15**(1), 114–119 (2009)
104. R. Cherif et al., Highly nonlinear As_2Se_3-based chalcogenide photonic crystal fiber for mid-infrared supercontinuum generation. Opt. Eng. **49**(9), 095002 (2010)
105. W.Q. Zhang et al., Fabrication and supercontinuum generation in dispersion flattened bismuth microstructured optical fiber. Opt. Express **19**(22), 21135–21144 (2011)
106. A. Marandi et al., Mid-infrared supercontinuum generation in tapered chalcogenide fiber for producing octave-spanning frequency comb around 3 μm. Opt. Express **20**(22), 24218–24225 (2012)
107. J.M. Dudley, G. Genty, S. Coen, Supercontinuum generation in photonic crystal fiber. Rev. Mod. Phys. **78**(4), 1135–1184 (2006)
108. J.M. Dudley, J.R. Taylor (eds.), *Supercontinuum Generation in Optical Fibers* (Cambridge University Press, Cambridge, 2010)
109. J.L. Krause, K.J. Schafer, K.C. Kulander, High-order harmonic-generation from atoms and ions in the high-intensity regime. Phys. Rev. Lett. **68**(24), 3535–3538 (1992)
110. A. Lhuillier, P. Balcou, High-order harmonic-generation in rare-gases with a 1-ps 1053-nm laser. Phys. Rev. Lett. **70**(6), 774–777 (1993)
111. P.B. Corkum, Plasma perspective on strong-field multiphoton ionization. Phys. Rev. Lett. **71**(13), 1994–1997 (1993)
112. M. Lewenstein et al., Theory of high-harmonic generation by low-frequency laser fields. Phys. Rev. A **49**(3), 2117–2132 (1994)

113. T. Popmintchev et al., The attosecond nonlinear optics of bright coherent X-ray generation. Nat. Photonics **4**(12), 822–832 (2010)
114. A.K. Mills et al., XUV frequency combs via femtosecond enhancement cavities. J. Phys. B, At. Mol. Opt. Phys. **45**(14), 142001 (2012)
115. D.C. Yost et al., Power optimization of XUV frequency combs for spectroscopy applications. Opt. Express **19**(23), 23483–23493 (2011)
116. M. Kourogi, K. Nakagawa, M. Ohtsu, Wide-span optical frequency comb generator for accurate optical frequency difference measurement. IEEE J. Quantum Electron. **29**(10), 2693–2701 (1993)
117. M. Kourogi, T. Enami, M. Ohtsu, A monolithic optical frequency comb generator. IEEE Photonics Technol. Lett. **6**(2), 214–217 (1994)
118. J. Ye et al., Highly selective terahertz optical frequency comb generator. Opt. Lett. **22**(5), 301–303 (1997)
119. S.A. Diddams et al., Broadband optical frequency comb generation with a phase-modulated parametric oscillator. Opt. Lett. **24**(23), 1747–1749 (1999)
120. T. Suzuki, M. Hirai, M. Katsuragawa, Octave-spanning Raman comb with carrier envelope offset control. Phys. Rev. Lett. **101**(24), 243602 (2008)
121. P. Del'Haye et al., Full stabilization of a microresonator-based optical frequency comb. Phys. Rev. Lett. **101**(5), 053903 (2008)
122. P. Del'Haye et al., Octave spanning tunable frequency comb from a microresonator. Phys. Rev. Lett. **107**(6), 063901 (2011)
123. T.J. Kippenberg, R. Holzwarth, S.A. Diddams, Microresonator-based optical frequency combs. Science **332**(6029), 555–559 (2011)
124. T.B.V. Herr, M.L. Gorodetsky, T.J. Kippenberg, Soliton mode-locking in optical microresonators. arXiv:1211.0733 (2012)
125. K. Saha et al., Modelocking and femtosecond pulse generation in chip-based frequency combs. Opt. Express **21**(1), 1335–1343 (2013)
126. S.B. Papp, S.A. Diddams, Spectral and temporal characterization of a fused-quartz-microresonator optical frequency comb. Phys. Rev. A **84**(5), 053833 (2011)
127. T. Herr et al., Universal formation dynamics and noise of Kerr-frequency combs in microresonators. Nat. Photonics **6**(7), 480–487 (2012)
128. L. Matos et al., Direct frequency comb generation from an octave-spanning, prismless Ti:sapphire laser. Opt. Lett. **29**(14), 1683–1685 (2004)
129. A. Bartels, D. Heinecke, S.A. Diddams, Passively mode-locked 10 GHz femtosecond Ti:sapphire laser. Opt. Lett. **33**(16), 1905–1907 (2008)
130. A. Ruehl et al., 80 W, 120 fs Yb-fiber frequency comb. Opt. Lett. **35**(18), 3015–3017 (2010)
131. I. Hartl et al., *Fully Stabilized GHz Yb-Fiber Laser Frequency Comb*. Advanced Solid State Phonics (Optical Society of America, Washington, 2009)
132. J. Rauschenberger et al., Control of the frequency comb from a mode-locked erbium-doped fiber laser. Opt. Express **10**(24), 1404–1410 (2002)
133. B.R. Washburn et al., Phase-locked, erbium-fiber-laser-based frequency comb in the near infrared. Opt. Lett. **29**(3), 250–252 (2004)
134. B.R. Walton et al., Transportable optical frequency comb based on a mode-locked fibre laser. IET Optoelectron. **2**(5), 182–187 (2008)
135. S. Herrmann et al., Atom optical experiments in the drop tower: a pathfinder for space based precision measurements, in *38th COSPAR Scientific Assembly* (2010)
136. F. Adler et al., Attosecond relative timing jitter and 13 fs tunable pulses from a two-branch Er:fiber laser. Opt. Lett. **32**(24), 3504–3506 (2007)
137. K. Moutzouris et al., Multimilliwatt ultrashort pulses continuously tunable in the visible from a compact fiber source. Opt. Lett. **31**(8), 1148–1150 (2006)
138. A. Gambetta, R. Ramponi, M. Marangoni, Mid-infrared optical combs from a compact amplified Er-doped fiber oscillator. Opt. Lett. **33**(22), 2671–2673 (2008)
139. N. Coluccelli et al., 250-MHz synchronously pumped optical parametric oscillator at 2.25–2.6 μm and 4.1–4.9 μm. Opt. Express **20**(20), 22042–22047 (2012)

140. D. Chao et al., Self-referenced erbium fiber laser frequency comb at a GHz repetition rate—OSA technical digest, in *Optical Fiber Communication Conference OW1C.2*, (2012)
141. F. Adler, S.A. Diddams, High-power, hybrid Er:fiber/Tm:fiber frequency comb source in the 2 μm wavelength region. Opt. Lett. **37**(9), 1400–1402 (2012)
142. R.A. Kaindl et al., Broadband phase-matched difference frequency mixing of femtosecond pulses in GaSe: experiment and theory. Appl. Phys. Lett. **75**(8), 1060–1062 (1999)
143. S.M. Foreman, D.J. Jones, J. Ye, Flexible and rapidly configurable femtosecond pulse generation in the mid-IR. Opt. Lett. **28**(5), 370–372 (2003)
144. C. Erny et al., Mid-infrared difference-frequency generation of ultrashort pulses tunable between 3.2 and 4.8 μm from a compact fiber source. Opt. Lett. **32**(9), 1138–1140 (2007)
145. L. Nugent-Glandorf et al., Mid-infrared virtually imaged phased array spectrometer for rapid and broadband trace gas detection. Opt. Lett. **37**(15), 3285–3287 (2012)
146. J.H. Sun, B.J.S. Gale, D.T. Reid, Composite frequency comb spanning 0.4–2.4 μm from a phase-controlled femtosecond Ti:sapphire laser and synchronously pumped optical parametric oscillator. Opt. Lett. **32**(11), 1414–1416 (2007)
147. D.T. Reid, B.J.S. Gale, J. Sun, Frequency comb generation and carrier-envelope phase control in femtosecond optical parametric oscillators. Laser Phys. **18**(2), 87–103 (2008)
148. S.T. Wong, K.L. Vodopyanov, R.L. Byer, Self-phase-locked divide-by-2 optical parametric oscillator as a broadband frequency comb source. J. Opt. Soc. Am. B, Opt. Phys. **27**(5), 876–882 (2010)
149. S. Marzenell, R. Beigang, R. Wallenstein, Synchronously pumped femtosecond optical parametric oscillator based on $AgGaSe_2$ tunable from 2 μm to 8 μm. Appl. Phys. B, Lasers Opt. **69**(5–6), 423–428 (1999)
150. E. Hecht, *Optics*, 3rd edn. (Addison-Wesley, Reading, 1998)
151. I. Hartl et al., Cavity-enhanced similariton Yb-fiber laser frequency comb: 3×10^{14} W cm^{-2} peak intensity at 136 MHz. Opt. Lett. **32**(19), 2870–2872 (2007)
152. R.J. Jones, I. Thomann, J. Ye, Precision stabilization of femtosecond lasers to high-finesse optical cavities. Phys. Rev. A **69**(5), 051803 (2004)
153. R.W.P. Drever et al., Laser phase and frequency stabilization using an optical-resonator. Appl. Phys., B Photophys. Laser Chem. **31**(2), 97–105 (1983)
154. T.W. Hansch, B. Couillaud, Laser frequency stabilization by polarization spectroscopy of a reflecting reference cavity. Opt. Commun. **35**(3), 441–444 (1980)
155. A. Foltynowicz et al., Quantum-noise-limited optical frequency comb spectroscopy. Phys. Rev. Lett. **107**(23), 233002 (2011)
156. A. Foltynowicz et al., Cavity-enhanced optical frequency comb spectroscopy in the mid-infrared application to trace detection of hydrogen peroxide. Appl. Phys. B **110**(2), 163–175 (2013)
157. R. Gebs et al., 1-GHz repetition rate femtosecond OPO with stabilized offset between signal and idler frequency combs. Opt. Express **16**(8), 5397–5405 (2008)
158. K.K. Lehmann, P.S. Johnston, P. Rabinowitz, Brewster angle prism retroreflectors for cavity enhanced spectroscopy. Appl. Opt. **48**(16), 2966–2978 (2009)
159. S. Kassi et al., Demonstration of cavity enhanced FTIR spectroscopy using a femtosecond laser absorption source. Spectrochim. Acta, Part A, Mol. Biomol. Spectrosc. **75**(1), 142–145 (2010)
160. R. Grilli et al., Frequency comb based spectrometer for in situ and real time measurements of IO, BrO, NO_2, and H_2CO at pptv and ppqv levels. Environ. Sci. Technol. **46**(19), 10704–10710 (2012)
161. R. Grilli et al., First investigations of IO, BrO, and NO_2 summer atmospheric levels at a coastal East Antarctic site using mode-locked cavity enhanced absorption spectroscopy. Geophys. Res. Lett. **40**, 1–6 (2013)
162. R. Grilli et al., Cavity-enhanced multiplexed comb spectroscopy down to the photon shot noise. Phys. Rev. A **85**(5), 051804 (2012)
163. M. Shirasaki, Large angular dispersion by a virtually imaged phased array and its application to a wavelength demultiplexer. Opt. Lett. **21**(5), 366–368 (1996)

164. S.A. Diddams, L. Hollberg, V. Mbele, Molecular fingerprinting with the resolved modes of a femtosecond laser frequency comb. Nature **445**(7128), 627–630 (2007)
165. J. Mandon, G. Guelachvili, N. Picque, Fourier transform spectroscopy with a laser frequency comb. Nat. Photonics **3**(2), 99–102 (2009)
166. S. Schiller, Spectrometry with frequency combs. Opt. Lett. **27**(9), 766–768 (2002)
167. I. Coddington, W.C. Swann, N.R. Newbury, Coherent multiheterodyne spectroscopy using stabilized optical frequency combs. Phys. Rev. Lett. **100**(1), 013902 (2008)
168. B. Bernhardt et al., Cavity-enhanced dual-comb spectroscopy. Nat. Photonics **4**(1), 55–57 (2010)
169. X.D.D. Vaernewijck et al., Cavity enhanced FTIR spectroscopy using a femto OPO absorption source. Mol. Phys. **109**(17–18), 2173–2179 (2011)
170. C. Gohle et al., Frequency comb vernier spectroscopy for broadband, high-resolution, high-sensitivity absorption and dispersion spectra. Phys. Rev. Lett. **99**(26), 263902 (2007)
171. T. Steinmetz et al., Laser frequency combs for astronomical observations. Science **321**(5894), 1335–1337 (2008)
172. T. Steinmetz et al., Fabry-Perot filter cavities for wide-spaced frequency combs with large spectral bandwidth. Appl. Phys. B, Lasers Opt. **96**(2–3), 251–256 (2009)
173. F. Quinlan et al., A 12.5 GHz-spaced optical frequency comb spanning >400 nm for near-infrared astronomical spectrograph calibration. Rev. Sci. Instrum. **81**(6), 063105 (2010)
174. A. Okeefe, D.A.G. Deacon, Cavity ring-down optical spectrometer for absorption-measurements using pulsed laser sources. Rev. Sci. Instrum. **59**(12), 2544–2551 (1988)
175. J.J. Scherer, Ringdown spectral photography. Chem. Phys. Lett. **292**(1–2), 143–153 (1998)
176. J.J. Scherer et al., Broadband ringdown spectral photography. Appl. Opt. **40**(36), 6725–6732 (2001)
177. S.M. Ball et al., Broadband cavity ringdown spectroscopy of the NO_3 radical. Chem. Phys. Lett. **342**(1–2), 113–120 (2001)
178. S.J. Xiao, A.M. Weiner, 2-D wavelength demultiplexer with potential for $\geq$1000 channels in the C-band. Opt. Express **12**(13), 2895–2902 (2004)
179. S.X. Wang, S.J. Xiao, A.M. Weiner, Broadband, high spectral resolution 2-D wavelength-parallel polarimeter for dense WDM systems. Opt. Express **13**(23), 9374–9380 (2005)
180. P.R. Griffiths, J.A. de Haseth, *Fourier Transform Infrared Spectrometry* (Wiley, Hoboken, 2007)
181. A.A. Ruth, J. Orphal, S.E. Fiedler, Fourier-transform cavity-enhanced absorption spectroscopy using an incoherent broadband light source. Appl. Opt. **46**(17), 3611–3616 (2007)
182. P. Balling et al., Length and refractive index measurement by Fourier transform interferometry and frequency comb spectroscopy. Meas. Sci. Technol. **23**(9), 094001 (2012)
183. J. Mandon et al., Femtosecond laser Fourier transform absorption spectroscopy. Opt. Lett. **32**(12), 1677–1679 (2007)
184. X.D.D. Vaernewijck, S. Kassi, M. Herman, (OCO)-O-17-C-12-O-17 and (OCO)-O-18-C-12-O-17 overtone spectroscopy in the 1.64 μm region. Chem. Phys. Lett. **514**(1–3), 29–31 (2011)
185. X.D.D. Vaernewijck, S. Kassi, M. Herman, (OCO)-O-17-C-12-O-17 and (OCO)-O-18-C-12-O-17 spectroscopy in the 1.6 μm region. Mol. Phys. **110**(21–22), 2665–2671 (2012)
186. P.C.D. Hobbs, Ultrasensitive laser measurements without tears. Appl. Opt. **36**(4), 903–920 (1997)
187. S.A. Davis, M. Abrams, J. Brault, *Fourier Transform Spectrometry* (Academic Press, San Diego, 2001), p. 262
188. A. Schliesser et al., Frequency-comb infrared spectrometer for rapid, remote chemical sensing. Opt. Express **13**(22), 9029–9038 (2005)
189. N.R. Newbury, I. Coddington, W. Swann, Sensitivity of coherent dual-comb spectroscopy. Opt. Express **18**(8), 7929–7945 (2010)
190. T. Ideguchi et al., Adaptive dual-comb spectroscopy in the green region. Opt. Lett. **37**(23), 4847–4849 (2012)

191. S. Boudreau, J. Genest, Referenced passive spectroscopy using dual frequency combs. Opt. Express **20**(7), 7375–7387 (2012)
192. J.D. Deschenes, P. Giaccari, J. Genest, Optical referencing technique with CW lasers as intermediate oscillators for continuous full delay range frequency comb interferometry. Opt. Express **18**(22), 23358–23370 (2010)
193. A. Schliesser, N. Picque, T.W. Hansch, Mid-infrared frequency combs. Nat. Photonics **6**(7), 440–449 (2012)
194. T.H. Risby, S.F. Solga, Current status of clinical breath analysis. Appl. Phys. B, Lasers Opt. **85**(2–3), 421–426 (2006)
195. L. Pauling et al., Quantitative analysis of urine vapor and breath by gas-liquid partition chromatography. Proc. Natl. Acad. Sci. USA **68**(10), 2374–2376 (1971)
196. A.J. Cunnington, P. Hormbrey, Breath analysis to detect recent exposure to carbon monoxide. Postgrad. Med. J. **78**(918), 233–237 (2002)
197. E.R. Crosson et al., Stable isotope ratios using cavity ring-down spectroscopy: determination of C-13/C-12 for carbon dioxide in human breath. Anal. Chem. **74**(9), 2003–2007 (2002)
198. B.J. Marshall, J.R. Warren, Unidentified curved bacilli in the stomach of patients with gastritis and peptic ulceration. Lancet **1**(8390), 1311–1315 (1984)
199. Helicobacter pylori: fact sheet for health care providers. Center for Disease Control, Atlanta, GA (1998)
200. S.Y. Lehman, K.A. Bertness, J.T. Hodges, Detection of trace water in phosphine with cavity ring-down spectroscopy. J. Cryst. Growth **250**(1–2), 262–268 (2003)
201. J. Feng, R. Clement, M. Raynor, Characterization of high-purity arsine and gallium arsenide epilayers grown by MOCVD. J. Cryst. Growth **310**(23), 4780–4785 (2008)
202. H.H. Funke et al., Techniques for the measurement of trace moisture in high-purity electronic specialty gases. Rev. Sci. Instrum. **74**(9), 3909–3933 (2003)
203. I. Horvath et al., Combined use of exhaled hydrogen peroxide and nitric oxide in monitoring asthma. Am. J. Respir. Crit. Care Med. **158**(4), 1042–1046 (1998)
204. S.A. Kharitonov, P.J. Barnes, Exhaled biomarkers. Chest **130**(5), 1541–1546 (2006)
205. S.A. Kharitonov, P.J. Barnes, Exhaled markers of pulmonary disease. Am. J. Respir. Crit. Care Med. **163**(7), 1693–1722 (2001)
206. P.S. Connell, D.J. Wuebbles, J.S. Chang, Stratospheric hydrogen-peroxide—the relationship of theory and observation. J. Geophys. Res., Atmos. **90**(Nd6), 10726–10732 (1985)
207. J.A. Snow et al., Hydrogen peroxide, methyl hydroperoxide, and formaldehyde over North America and the North Atlantic. J. Geophys. Res., Atmos. **112**(D12), D12s07 (2007)
208. C.P. Rinsland et al., Detection of elevated tropospheric hydrogen peroxide (H_2O_2) mixing ratios in atmospheric chemistry experiment (ACE) subtropical infrared solar occultation spectra. J. Quant. Spectrosc. Radiat. Transf. **107**(2), 340–348 (2007)
209. T.J. Johnson et al., Absolute integrated intensities of vapor-phase hydrogen peroxide (H(2)O(2)) in the mid-infrared at atmospheric pressure. Anal. Bioanal. Chem. **395**(2), 377–386 (2009)
210. J.D. Rogers, Calculation of absolute infrared intensities of binary overtone, combination, and difference bands of hydrogen-peroxide. J. Phys. Chem. **88**(3), 526–530 (1984)
211. L.S. Rothman et al., The HITRAN 2008 molecular spectroscopic database. J. Quant. Spectrosc. Radiat. Transf. **110**(9–10), 533–572 (2009)
212. R. Ciurylo, Shapes of pressure- and Doppler-broadened spectral lines in the core and near wings. Phys. Rev. A **58**(2), 1029–1039 (1998)
213. J.-M. Hartmann, C. Boulet, D. Robert, *Collisional Effects on Molecular Spectra: Laboratory Experiments and Model, Consequences for Applications* (Elsevier, Amsterdam, 2008)
214. T.A. Staffelbach et al., Comparison of hydroperoxide measurements made during the Mauna Loa observatory photochemistry experiment 2. J. Geophys. Res., Atmos. **101**(D9), 14729–14739 (1996)
215. P.J. Sarre, The diffuse interstellar bands: a major problem in astronomical spectroscopy. J. Mol. Spectrosc. **238**(1), 1–10 (2006)

216. T.P. Snow, V.M. Bierbaum, Ion chemistry in the interstellar medium. Annu. Rev. Anal. Chem. **1**, 229–259 (2008)
217. S. Schiller, V. Korobov, Tests of time independence of the electron and nuclear masses with ultracold molecules. Phys. Rev. A **71**(3), 032505 (2005)
218. E.R. Meyer, J.L. Bohn, M.P. Deskevich, Candidate molecular ions for an electron electric dipole moment experiment. Phys. Rev. A **73**(6), 062108 (2006)
219. J.C.J. Koelemeij et al., Vibrational spectroscopy of HD^+ with 2-ppb accuracy. Phys. Rev. Lett. **98**(17), 173002 (2007)
220. L.V. Skripnikov et al., On the search for time variation in the fine-structure constant: ab initio calculation of HfF^+. JETP Lett. **88**(9), 578–581 (2008)
221. K. Beloy et al., Rotational spectrum of the molecular ion NH^+ as a probe for alpha and $m(e)/m(p)$ variation. Phys. Rev. A **83**(6), 062514 (2011)
222. A.E. Leanhardt et al., High-resolution spectroscopy on trapped molecular ions in rotating electric fields: a new approach for measuring the electron electric dipole moment. J. Mol. Spectrosc. **270**(1), 1–25 (2011)
223. B.J. Barker et al., Communication: spectroscopic measurements for HfF^+ of relevance to the investigation of fundamental constants. J. Chem. Phys. **134**(20), 201102 (2011)
224. B.J. Barker et al., Spectroscopic investigations of ThF and ThF^+. J. Chem. Phys. **136**(10), 104305 (2012)
225. A.N. Petrov, N.S. Mosyagin, A.V. Titov, Theoretical study of low-lying electronic terms and transition moments for HfF^+ for the electron electric-dipole-moment search. Phys. Rev. A **79**(1), 012505 (2009)